Title	Stress concentration factor prediction by the multi-dimensional Lagrangian interpolation method
Author(s)	Lee, Chi King; Chiew, Sing Ping; Lie, Seng Tjhen; Sopha, T.
Citation	Lee, C. K., Chiew, S. P., Lie, S. T., & Sopha, T. (2011). Stress concentration factor prediction by the multi-dimensional Lagrangian interpolation method. Engineering Fracture Mechanics, 78(6), 1008-1028.
Date	2011
URL	http://hdl.handle.net/10220/18893
Rights	© 2011 Elsevier. This is the author created version of a work that has been peer reviewed and accepted for publication by Engineering Fracture Mechanics, Elsevier. It incorporates referee's comments but changes resulting from the publishing process, such as copyediting, structural formatting, may not be reflected in this document. The published version is available at: [DOI:http://dx.doi.org/10.1016/j.engfracmech.2010.11.013].

Pre-printed version of the paper published in the journal: Engineering Fracture Mechanics, Vol. 78, pp1008-1028, 2011

STRESS CONCENTRATION FACTOR PREDICTION BY THE MULTI-DIMENSIONAL LAGRANGIAN INTERPOLATION METHOD

[1]*C. K. Lee, S. P. Chiew, S. T. Lie and T. Sopha*

School of Civil and Environmental Engineering

Nanyang Technological University

50 Nanyang Avenue, Singapore 639798

Abstract

A new approach based on the multi-dimensional Lagrangian interpolation method, which is widely used in the finite element method, is proposed for the prediction of stress concentration factor for tubular joints. When comparing with the parametric regression method, this new method uses the same set of numerical parametric study results as its inputs. The accuracy of the proposed method is validated by applying it to predict the stress concentration factor and hot spot stress of partially overlapped circular hollow section K-joints. Numerical results indicated that the new method is more reliable and accurate than the parametric regression method.

Keywords: Stress concentration factor, hot spot stress, multi-dimensional Lagrangian interpolation method, partially overlapped CHS K-joints

[1] Corresponding Author

Email: ccklee@ntu.edu.sg Tel: 65-67905293 Fax: 65-67921650

1. Introduction

The geometrical stress method [1] is a popular approach for fatigue assessment of structural tubular joints. One main step of the geometrical stress method is to determine the *hot spot stress (HSS)* of the joint under the applied loads. The HSS is then checked with the S-N curves [1] for fatigue life estimation. To facilitate design works, the concept of *stress concentration factor (SCF)*, which is defined as the ratio between the HSS and the corresponding nominal stress induced by the applied loads, is widely used [1,2]. In fatigue assessments, the SCFs under different loading cases are first determined and the HSS induced could then be estimated by combining the SCFs with the corresponding nominal stresses. While the SCF for any joint type could be determined by experimental study [3,4] or by finite element (FE) modellings [5,6], due to the high cost and long time needed, these two methods are seldom used in everyday design works. In practice, all design guidelines [1,2] provide empirical equations of SCF for commonly used joint types. These empirical equations are normally obtained by the following steps:

(1) Conduct some carefully designed tests which are within the interested geometrical ranges of the targeted joint type.

(2) Develop numerically models to predict the responses of the targeted joint type. The correctness and reliability of the models are validated by comparing modelling results with experimental results.

(3) Carry out a *numerical parametric study (NPS)* using the validated numerical model to determine the variations of SCF over the interested geometrical ranges. Usually, the effects of axial loading (AX) and in-plane-bending (IPB) will be studied separately.

(4) Based on the results obtained from the NPS, a set of empirical SCF equations are constructed. Currently, nearly all empirical SCF equations were obtained by applying the multi-variable *parametric regression method (PRM)* on the NPS results. Usually, fitting

parameters which are believed to be critically affecting the SCF were used in the regression.

It should be mentioned that the application ranges of the empirical equations are solely depended on the range of the geometrical parameters employed in the NPS. Furthermore, depend on the regression method adopted and the number of fitting parameters included, empirical equations with very different accuracy could be created from the *same* NPS. While the accuracy of the empirical equations could be improved by including more fitting parameters, this could lead to the following problems.

(1) For complex joint types under complex loadings, the use of more fitting parameters will result in lengthy equations [7].

(2) After all critical fitting parameters are included, the accuracy of the empirical equation could not be improved effectively by adding more parameters nor by increasing the number of numerical models of the NPS [8].

The main objective of this paper is to suggest an alternative procedure for the prediction of SCF and HSS for tubular joints. The essence of this new approach is to give up the PRM and the empirical equations entirely. A new method based on the *multi-dimensional Lagrangian interpolation (MLI)* method is suggested. In this procedure, the MLI functions, which are the generalized form of the shape functions used in FE analysis [9], are employed. It would be shown that much improvements in the accuracy of SCF and HSS predictions could be achieved by bringing this well accepted approach from the field of FE analysis to the field of structural steel design where most of the SCF and HSS predictions are still based on regression analyses. Note that the idea of using the MLI functions in tubular joint works was originated by Shao et al. [8,10,11] when he was a member of the research team leaded by the first three authors [10]. The work reported by Shao [8,11] was on the prediction the maximum stress intensity factor for gapped CHS K-joints. In this paper, the application of the MLI

method will be extended to the prediction of both single value (e.g. maximum SCF and HSS) and multi-value responses (e.g. HSS distributions). In order to explain the working principle and to validate the reliability of the method, a study involving SCF and HSS predictions for partially overlapped CHS K-joints is presented.

In the next section, the theory of the MLI method is given. It is then followed by summaries of the NPS conducted and the empirical equations obtained. After that, descriptions on how to apply the MLI method for SCF and HSS predictions for partially overlapped CHS K-joints are given. A numerical study is then presented to validate the accuracy of the MLI method. Finally, conclusions of the study are given.

2 The multi-dimensional Lagrangian interpolation method

The main concept of this approach is that since the key responses over the selected geometrical ranges and loading parameters at some fixed intervals are already computed during the NPS, the Lagrangian interpolation functions, which are well adopted in FE analysis [9] could be employed to construct an *interpolation* approximation of key responses of the targeted joint type.

The simple 1D case is shown in Fig. 1. The response Φ (e.g. SCF) is a function of the parameter ξ in the range [ξ_1, ξ_8]. The values of Φ at the non-uniformly spaced nodes, ξ_i, i=1,..,8 are denoted as Φ_i and have been obtained during the NPS. If the value of Φ at a point $\xi=\xi_{eval}$ is required, the third interval [ξ_3, ξ_4] that contains ξ_{eval} is identified. The approximated value $\tilde{\Phi}(\xi_{eval})$ is then computed as

$$\tilde{\Phi}(\xi_{eval}) = L_1(\xi_{eval})\Phi_3 + L_2(\xi_{eval})\Phi_4 \tag{1}$$

In Eqn. (1), $L_j(\xi)$, j=1, 2 are the first order Lagrangian interpolation function [9] defined as

$$L_1(\xi) = \frac{\xi_{i+1} - \xi}{\xi_{i+1} - \xi_i}, \quad L_2(\xi) = \frac{\xi - \xi_i}{\xi_{i+1} - \xi_i}, i = 3 \tag{2}$$

For the 2D case (Fig. 2), Φ is a function of two parameters ξ^1 and ξ^2 and the point $(\xi^1_{eval}, \xi^2_{eval})$ is enclosed by $2^2=4$ nodal points. To obtain $\tilde{\Phi}\left(\xi^1_{eval}, \xi^2_{eval}\right)$, the approximated value of Φ at $(\xi^1_{eval}, \xi^2_{eval})$, one needs to first identify the i_1th interval along the ξ^1 axis and the i_2th interval along the ξ^2 axis that enclosing $(\xi^1_{eval}, \xi^2_{eval})$. $\tilde{\Phi}\left(\xi^1_{eval}, \xi^2_{eval}\right)$ can then be expressed as

$$\begin{aligned}\tilde{\Phi}\left(\xi^1_{eval}, \xi^2_{eval}\right) = L^1_1\left(\xi^1_{eval}\right)L^2_1\left(\xi^2_{eval}\right)\Phi_{i_1,i_2} + L^1_2\left(\xi^1_{eval}\right)L^2_1\left(\xi^2_{eval}\right)\Phi_{i_1+1,i_2} + \\ L^1_1\left(\xi^1_{eval}\right)L^2_2\left(\xi^2_{eval}\right)\Phi_{i_1,i_2+1} + L^1_2\left(\xi^1_{eval}\right)L^2_2\left(\xi^2_{eval}\right)\Phi_{i+1_1,i_2+1}\end{aligned} \tag{3}$$

where
$$L^k_1\left(\xi^k\right) = \frac{\xi^k_{i_k+1} - \xi^k}{\xi^k_{i_k+1} - \xi^k_{i_k}}, \quad L^k_2\left(\xi^k\right) = \frac{\xi^k - \xi^k_{i_k}}{\xi^k_{i_k+1} - \xi^k_{i_k}}, k = 1,2 \tag{4}$$

are defined within the ranges of $[\xi^1_1, \xi^1_{m_1}]$ and $[\xi^2_1, \xi^2_{m_2}]$. Eqn. 3 could be expressed in a more compact form as

$$\tilde{\Phi}\left(\xi^1_{eval}, \xi^2_{eval}\right) = \sum_{\alpha_1,\alpha_2=1,2}^{\alpha_1+\alpha_2\le 4} L^1_{\alpha_1}\left(\xi^1_{eval}\right)L^2_{\alpha_2}\left(\xi^2_{eval}\right)\Phi_{i_1+\alpha_1-1,i_2+\alpha_2-1} \tag{5}$$

In the FE method [9], such interpolation procedure is routinely carried out up to the 3D case. However, for complex tubular joint, it is necessary to extend the method to higher dimension. In general, the M-dimensional case shall involve M parameters ξ^k which are defined in the intervals $[\xi^k_1, \xi^k_{m_k}]$ for k=1,….,M. The point of evaluation $\boldsymbol{\xi}_{eval}=(\xi^1_{eval}, \xi^2_{eval}, ..., \xi^M_{eval})$ is now enclosed by a *hyper-rectangle* with 2^M nodes defined by M intervals $[\xi^k_{i_k}, \xi^k_{i_{k+1}}]$ such that $\xi^k_{i_k} \le \xi^k_{eval} \le \xi^k_{i_{k+1}}$. The expression of the approximated value at $\boldsymbol{\xi}_{eval}$, $\tilde{\Phi}\left(\boldsymbol{\xi}_{eval}\right)$, is given by

$$\tilde{\Phi}\left(\boldsymbol{\xi}_{eval}\right) = \sum_{\alpha_k=1,2,k=1,..M}^{\sum\alpha_k\le 2M}\left(\prod_{k=1}^{M} L^k_{\alpha_k}\left(\xi^k_{eval}\right)\right)\Phi_{i_k+\alpha_k-1} \tag{6}$$

In Eqn. 6, $\Phi_{i_k+\alpha_k-1}$ denotes the known nodal value of Φ at $(\xi^1_{i_1+\alpha_1-1}, \xi^2_{i_2+\alpha_2-1}, ..., \xi^k_{i_M+\alpha_M-1})$, $L^k_{\alpha_k}$ is the corresponding first order Lagrangian interpolation function defined in Eqn. 4 while

$\left(\prod_{k=1}^{M} L_{\alpha_k}^k\left(\xi_{eval}^k\right)\right)$ are the MLI functions for the *M*-dimensional space that has the following properties.

(1) Interpolatant condition

The functions $L_{\alpha_k}^k\left(\xi^k\right)$ and $\left(\prod_{k=1}^{M} L_{\alpha_k}^k\left(\xi^k\right)\right)$ satisfies the *interpolatant* condition such that [9]

$$\prod_{k=1}^{M} L_{\alpha_k}^k\left(\xi_{i_k+j-1}^k\right) = \delta_{\alpha_k,j} = \begin{cases} 1, \ for\ \alpha_k = j \\ 0, for\ \alpha_k \neq j \end{cases}, \quad \alpha_k, j = 1,2 \tag{7}$$

Eqn. 7 implies that the MLI method *always* returns the exact pre-computed value of $\Phi_{i_k+\alpha_k-1}$ when $\boldsymbol{\xi_{eval}} = (\xi_{i_1+\alpha_1-1}^1, \xi_{i_2+\alpha_2-1}^2, ..., \xi_{i_M+\alpha_M-1}^k)$.

(2) Convergence

From the error estimation of the FE method, it could be shown [9,11] that if Φ is a smooth function of ξ^k, the error of the MLI method is proportional to the size of the hyper-rectangle. That is, for any arbitrary point $\boldsymbol{\xi_{eval}}$ within the parametric range, the error of the approximation, $\left|\tilde{\Phi}\left(\xi_{eval}\right) - \Phi\left(\xi_{eval}\right)\right|$, is given by

$$\left|\tilde{\Phi}\left(\xi_{eval}\right) - \Phi\left(\xi_{eval}\right)\right| \leq C\, max(h_k^2)\ for\ k = 1,...,M \tag{8}$$

where $h_k = \xi_{i_{k+1}}^k - \xi_{i_k}^k, k = 1,...,M$ are the edge lengths of the hyper-rectangle contains $\boldsymbol{\xi_{eval}}$. Eqn. 8 implies that the accuracy of the prediction could be improved by employing more models in the NPS to reduce the spacing of the parametric points.

(3) Computational cost

From Eqns. 6, it could be seen that once the hyper-rectangle enclosing $\boldsymbol{\xi_{eval}}$ is identified, the computational cost to evaluate $\tilde{\Phi}\left(\boldsymbol{\xi_{eval}}\right)$ is only proportional to *M*. Furthermore, to identify the hyper-rectangle enclosing $\boldsymbol{\xi_{eval}}$, a linear search with a complexity of $O(\max(m_M))$ is sufficient.

Hence, the computational cost for the evaluation of $\tilde{\Phi}(\xi_{eval})$ is modest when comparing with the cost of the NPS.

(4) Single and multiple responses values

One advantage of the MLI method over the PRM is that Eqn. 6 is applicable to any response at any part of the structures. This allows the estimation of multiple response values (or the distributions of the responses) over some critical regions of the joint. Such extension could be done by selecting an additional parameter that defines the locations of the response. Fig. 3 shows an example for the SCF distribution along the brace-chord intersection of a tubular joint. The usual practice of the PRM is to store the maximum SCF at the crown of the joint only. However, in the MLI method, it is possible to store a set of SCF values along the brace-chord intersection curve. In Fig. 3, the driving angle φ is selected as the parameter to define the locations of the SCF values. In practice, by using an automatic mesh generation procedure [12], it is easy to generate a series of similar FE meshes in the NPS so that SCF values corresponding to the same set of φ_i are obtained.

3 Parametric numerical study on partially overlapped CHS K-joint

3.1 Range of NPS and FE models

Fig. 4 shows the nine geometrical parameters (θ_1, θ_2, α, γ, O_v, β_1, τ_1, β_2 and τ_2) that are needed to define the geometry of a partially overlapped CHS K-joint [12]. If five different values for these parameters are adopted, an impractical number of $5^9 \approx 0.2$ million joints are needed. Hence, in this study, only partially overlapped CHS K-joints with identical through and overlap braces (i.e. $\beta_1=\beta_2=\beta$ and $\tau_1=\tau_2=\tau$) and with the same intersecting angles between chord and braces (i.e. $\theta_1=\theta_2=\theta$) are considered. While the α value may has much affect on SCF, only a constant value of $\alpha=6$, which corresponding to the condition of an internal joint and the full scale tests done during previous experimental studies [10], is used. After adopted

these simplifications, the number of geometrical parameters is reduced to five (θ, γ, O_v, β, τ) and leaded to 3500 joints in this study (Table 1). In the NPS, six different AX and IPB loading cases were considered (Fig. 5). Obviously, it is impractical to discretize the 3500 joints into FE meshes manually. Hence, an automatic procedure [12] was developed for mesh generation. Furthermore, this ensures that meshes with similar pattern are generated for all joints and allows a database for multiple key responses values to be created. A typical FE mesh used in the NPS is shown in Fig. 5.

Note that in Table 1, the range of $\gamma=R_0/t_0$ was selected so it is corresponding to the dimensions of those commonly used CHS. In addition, for different γ values, different ranges of $\tau=t_1/t_0$ were employed to tidy with those CHS sizes used in practice. Such practical choices of parametric values results in a trapezoidal interpolation gird. Hence, the MLI functions are slightly modified accordingly (Appendix A).

3.2 Parametric regression analyses and empirical SCF equations

In order to construct the empirical SCF equations, the maximum SCF obtained from the 3500 models are compiled according to the five selected geometrical parameters, the six basic loading cases and the chord and braces sides of the three intersection curves (Fig. 5). For each model, sixteen maximum SCF values (six from the through brace, six from the overlap brace and four from the chord) are stored (Fig. 6). Thus, 16×3500=56000 SCF values are used to derive the empirical SCF equations. For each FE model, as shown in Fig. 6, the maximum SCF values obtained are labelled according to the basic load cases applied (e.g. AX11, AX21, IPB11 etc) and the side (“c” for chord, “t” for through brace and “o” for overlap brace) where its values on the intersection curves (Curves A, B and C) is recorded. For example, the maximum SCF along the through brace side of intersection Curve C under IPB11 is denoted as IPB11tC.

Note that for AX11, four SCFs (AX11tA, AX11oA, AX11tC and AX11cC) are recorded despites that the values corresponding to AX11tA and AX11oA are not the maximum SCF for AX11. Similarly, for AX21, four SCFs (AX21oA, AX21tA, AX22oB and AX22cB) are recorded despites that the values corresponding to AX21oA and AX21tA are not the maximum SCF for AX21.

For the construction of the empirical SCF equations, it was found that the simple linear regression model suggested by Sabih [13] yields the best empirical SCF equations from the NPS results. Detailed expressions for the empirical SCF equations obtained for the partially overlapped CHS K-joints could be found in reference [14].

In this study, the accuracy of the PRM is assessed by the following two approaches:

(1) Assessment using the P/R ratio

According to the Fatigue Guidance Review Panel guideline [15], the reliability of the empirical equations is assessed by computing the ratio between the predicted SCF from the empirical equations (the "P" values) and the SCF from the FE solutions (the "R" values) for all the models used in the NPS. If the P/R ratios for most cases are closed to unity, the reliability of the equation is assured. However, the equations are commented to underestimate and overestimate the SCF if the P/R ratios are outside the range of [0.8, 1.5]. Table 2 shows the distributions of the P/R ratios for the empirical SCF equations. It is observed that the highest and lowest percentages of the P/R ratios that fall in the range of [0.8, 1.5] are 90.54% and 70.45%, respectively. Thus, it appears that the empirical equations are reasonably accurate.

(2) Assessment using mid-point models

As the empirical equations will be employed to predict the maximum SCFs for joints that are not used in the NPS, a more thorough way to assess their accuracies is to compare their predictions with the maximum SCFs obtained from some "mid-point" models. These mid-

point models are created by using geometrical parameters that are corresponding to the mid values of those used in the NPS. For example, the θ values of the mid-point models are 35° and 55° which are corresponding to the values of (30°, 40°) and (50°, 60°) used in the NPS, respectively. A total of 192 such mid-point models are constructed and their geometrical parameters are listed in Table 3. The relative error between the SCFs predicted by the empirical equations (SCF_{PRM}) and the corresponding values from the FE solutions (SCF_{FEM}) of these mid-point models, $E_{PRM\text{-}FEM}(SCF)$, is defined as:

$$E_{PRM-FEM}(SCF) = \frac{SCF_{PRM} - SCF_{FEM}}{SCF_{PRM}} \times 100\% \tag{9}$$

Table 4 shows the distributions of the relative error $E_{PRM\text{-}FEM}(SCF)$ for the mid-point models. It can be seen that the highest and lowest percentages of $E_{PRM\text{-}FEM}(SCF)$ that are within the range of [-20%, 20%] are 94.08% and 44.74%, respectively. While it appears that on average the empirical equations still show reasonable accuracy, in some cases, extensive overestimations (e.g. AX11cC, AX21oB and IPB21cB) and underestimations (e.g. IPB11cC and IPB21cB) appeared.

4 Applications of the MLI method for the predictions of SCF and HSS

In this section, the MLI method is applied for SCF and HSS predictions. Two different methods, namely the *Point Interpolation Method (PIM)* and the *Line Interpolation Method (LIM)* are developed based on the MLI functions.

4.1 The point interpolation method (PIM)

The basic concept of PIM is simple, rather than using regression analysis to generate empirical equations, estimations of maximum SCFs could be computed directly using the MLI method (Eqn. 6 with five parameters θ, γ, p, β and τ) based on the 56000 SCFs obtained from the NPS. Since the MLI functions satisfy the interpolatant condition (Eqn. 7) and give

exact predictions for models used in the NPS, its accuracy could not be assessed using the P/R ratio. Hence, the accuracy of the PIM is assessed by the 192 mid-point models (Table 3) which were *not* employed for the construction of the MLI functions. The relative error between the SCF estimated by the PIM (SCF_{PIM}) and the corresponding values from the FE analyses (SCF_{FEM}) for the mid-point models, $E_{PIM\text{-}FEM}(SCF)$, is defined as:

$$E_{PIM-FEM}(SCF) = \frac{SCF_{PIM} - SCF_{FEM}}{SCF_{PIM}} \times 100\% \tag{10}$$

Table 5 shows the distribution of $E_{PIM\text{-}FEM}(SCF)$ for the 192 mid-point models. It is obvious that the PIM outperformed the PRM in all the loading cases and virtually all relative errors fall within the range of [-20%, 20%]. The relative error distributions obtained from the PRM and the PIM are shown in Figs. 7 to 12. The relative error distributions for the PRM are much wider than the PIM, especially for the cases of AX11, AX21 and IPB11. Since in the PIM, the same set of SCFs was used, such improvement is solely due to the use of the MLI method.

Besides SCF prediction, both the PIM and the PRM could be employed for the estimation of the HSS when the joint is subjected to combined loadings. A simple and conservative prediction of the HSS could be obtained by using the following expression [16]:

$$HSS = \left|SCF_{AX} \times f_{AX}\right| + \left|SCF_{IPB} \times f_{IPB}\right| \tag{11}$$

where SCF_{AX} and SCF_{IPB} are the maximum SCFs for the AX and the IPB loadings, respectively. f_{AX} and f_{IPB} are their corresponding nominal stresses. Eqn. 11 shall give reasonably conservative prediction for the HSS if the maximum SCFs induced by different basic loadings are located at similar locations on the same intersection curve and the variation of the SCF is small. An example for the combined loading AX11(100kN)+IPB11(12kNm) is shown in Fig. 13 when the maximum SCFs for both AX11 and IPB11 occurred on Curve C.

However, such same curve, similar location and small variation conditions are not always occurred. Hence, in order to improve the accuracy of the PIM when the maximum SCFs corresponding to different loadings are located at different intersection curves, additional

SCFs for AX11 and AX21 at the through and overlap braces (AX11tA and AX11oA for the AX11 load case, AX21tA and AX21oA for the AX21 load case, see Section 3.2) are stored. These additional SCFs allow the PIM to give a better HSS prediction by selecting the appropriate SCFs when evaluating Eqn. 11. Fig. 14 shows how such procedure could avoid unnecessary overestimation for the combined loading AX11(100kN)+IPB12(12kNm). In this case, the IPB12 and the AX11 induce maximum SCF on Curves A and C, respectively. However, from FE analysis, it is found that the HSS (HSS_{FEM}=96.12N/mm^2) is caused by the combination of *both* AX11 and IPB12 on Curve A. Fig. 14 shows that if the HSS is estimated by summing up the contribution from Curve A (for IPB12) and Curve C (for AX11), an overestimated value of 128.21N/mm^2 will be obtained. However, by storing the SCF for AX11 along Curve A, a much better estimation of HSS_{PIM}=96.74N/mm^2 is obtained.

The reliability of the PIM for HSS prediction is assessed by applying it to the 192 mid-point models for the following four combined loadings:

1. AX11(100kN)+IPB11(12kNm)
2. AX11(100kN)+IPB12(12kNm)
3. AX21(100kN)+IPB21(12kNm)
4. AX21(100kN)+IPB22(12kNm)

The accuracies of the predicted HSS for the 192 mid-point models are obtained by using the PRM and the PIM are assessed by the following relative errors:

For the PIM: $$E_{PIM-FEM}(HSS) = \frac{HSS_{PIM} - HSS_{FEM}}{HSS_{PIM}} \times 100\% \quad (12a)$$

For the PRM: $$E_{PRM-FEM}(HSS) = \frac{HSS_{PRM} - HSS_{FEM}}{PHSS_{PRM}} \times 100\% \quad (12b)$$

In Eqn. 12, HSS_{PRM}, HSS_{PIM} and HSS_{FEM} are the HSS obtained by using the PRM, the PIM and the FE analysis, respectively. Figs. 15 to 18 and Table 6 show the relative error

distributions for the 192 mid-point models. It can be seen that the PIM outperformed the PRM in all cases.

4.2 The line interpolation method (LIM)

Despite that when comparing with the PRM, the PIM reduces the number of extensive overestimation in all loading cases, Table 6 shows that for AX21(100kN)+IPB21(12kNm), there are still more than 10% predictions with relative errors higher than 20%. Careful investigations of these cases indicated that while the maximum SCFs induced by AX21 and IPB21 are both located at the chord side of Curve B, they often occur at the two extreme ends of the curve with very different values (Figs. 19a and 19b). Fig. 19c indicates that if Eqn. 11 is used, extensive overestimated value of HSS_{PIM} is obtained. Fig. 19c also indicates that HSS actually locates at the middle part of the curve and its value could be estimated accurately by superimposing the HSS distributions of the two loading cases.

The above example indicates that the superposition method [17] could be employed to further reduce cases of extensive overestimation. For the superposition method, the stress distribution along an intersection curve $\sigma(\varphi)$ is expressed as:

$$\sigma(\varphi) = \hat{\sigma}_{AX}(\varphi) f_{AX} + \hat{\sigma}_{IPB}(\varphi) f_{IPB} \tag{13}$$

In Eqn. 13, $\hat{\sigma}_{AX}(\varphi)$ and $\hat{\sigma}_{IPB}(\varphi)$ are the SCF distributions along the intersection curve under the AX and IPB, respectively. φ is a geometrical parameter defining the locations of the interested point along the curve. In this study, the driving angle φ (Fig. 3) which is used in the mesh generation [12] is adopted. In practice, since no analytical form of the SCF distribution is available, approximated values could be obtained by first carry out FE analyses and then use the extrapolation method [1] to extract their values at a set of selected points φ_i on the intersection curve (Fig. 20). From this set of extracted values, a *line interpolation* approximation of the SCF distribution, $\hat{\sigma}_{LC}(\varphi)$, could be constructed so that

$$\hat{\sigma}_{LC}(\varphi) \approx \sum_{i=1}^{NSP} \hat{N}_i(\varphi)\hat{\sigma}_{LC}^{FEM}(\varphi_i),\ LC = AX \text{ or } IPB \tag{14}$$

In Eqn. 14, *NSP* is the number of selected points at which the SCF is extracted. $\hat{\sigma}_{LC}^{FEM}(\varphi_i)$ is the extracted SCF for the loading case *LC=AX or IPB* at the *i*th selected point with parametric coordinate φ_i. $\hat{N}_i(\varphi)$ is the interpolation function corresponding to φ_i constructed by using the 1D Lagrangian interpolation functions (Eqn. 2). Hence, if the values of $\hat{\sigma}_{LC}^{FEM}(\varphi_i)$ for *all* the intersection curves are known, Eqns. 13 and 14 could be used to predict the value of HSS. In practice, for a joint with arbitrary geometrical parameters, values of $\hat{\sigma}_{LC}^{FEM}(\varphi_i)$ could be obtained by carrying out 3D FE analysis. However, such a task is too expensive for everyday design works. In here, a new approach of LIM is suggested to carry out the superposition procedure. The main idea is to first use the PIM to estimate the values of $\hat{\sigma}_{LC}^{FEM}(\varphi_i)$ along the intersection curves. Eqns. 13 and 14 are then employed to construct the HSS distributions. In the LIM, interpolations are first carried out among different joint models to obtain $\hat{\sigma}_{LC}^{FEM}(\varphi_i)$ and then along the intersection curve (Eqn. 14). Comparing with the PIM, more data must be stored and a more complex calculation procedure is required. Boxes 1 and 2 summarize the storage scheme and the interpolation procedure for the LIM.

(1) Use the automatic mesh generator [12] to create 3D meshes for the joint models.
(2) Carry out the NPS.
(3) Extrapolate and extract the SCF from the midpoint of the elements along the intersection curves (Fig. 20). For the meshes using in this study, 14 to 25 SCFs are stored for each intersection curve.
(4) The SCF extracted are then stored in different files which are organized in a multilayered database according to the geometrical properties of the joints to increase the searching efficiency (Fig. 21).

Box1. Storage scheme for the LIM

(1) Input the geometrical parameters of the target joint and the loading conditions.
(2) Retrieve those joints which form the hyper-rectangle that enclosing the target joint.
(3) Construct the MLI functions (Eqn. 6).
(4) For each basic loading, retrieve the SCF distributions for all enclosing joints.
(5) For each basic loading, compute $\hat{\sigma}_{LC}^{FEM}(\varphi_i)$ for the target joint using the PIM.
(5) Use Eqns. 13 and 14 to combine the effect of different basic loadings to obtain the HSS distributions along all intersection curves of the target joint
(7) Scan through the HSS distributions to determine the HSS.

Box 2. Interpolation procedure for the LIM

It is found that for the database created from the 3500 joints used in this study, the interpolation and the HSS estimation obtained by the LIM (HSS_{LIM}) could be completed in a short time (<0.02s) on a low end notebook computer. Figs. 15 to 18 and Table 6 show the distributions of $E_{LIM\text{-}FEM}(HSS)$, the relative error of HSS_{LIM}, which is defined as

$$E_{LIM-FEM}(HSS) = \frac{HSS_{LIM} - HSS_{FEM}}{HSS_{LIM}} \times 100\% \quad (15)$$

for the 192 mid-point models. It can be seen that the LIM outperformed both the PRM and the PIM consistently. Furthermore, when comparing with the PIM, significant improvements were obtained for the combined loading cases of AX11(100kN)+IPB11(12kNm) and AX21(100kN)+IPB21(12kNm). In both cases, the numbers of models with relative error greater than 20% were reduced to less than 4% of the total numbers of models studied.

5 Conclusions

In this paper, a new approach for the estimation of the stress concentration factor (SCF) and the hot spot stress (HSS) for tubular joint is suggested. This new method, which is based on the multi-dimensional Lagrangian interpolation (MLI) functions that are widely used in finite element analysis, only requires the analysis results from a numerical parametric study and does not require additional input data when comparing with the traditional parametric regression method (PRM). Based on this new approach, two estimation procedures, namely

the point interpolation method (PIM) and the line interpolation methods (LIM) are suggested. In the PIM, only the maximum SCFs for the intersection curves are stored and used in SCF estimation. Furthermore, by assuming that the maximum SCFs induced by different basic loadings are located at the same position, it gives conservative estimation of the HSS under combined loadings. In the LIM, the SCF distributions along the intersection curves of the joints are stored in a carefully designed database. This information is then combined with the PIM and the superposition principle for HSS predictions. Numerical examples indicated that both the PIM and the LIM gave much better SCF and HSS predictions than the PRM. Moreover, when comparing with the PIM, the LIM gave more accurate HSS predictions with less overestimation. Both the PIM and the LIM only require little computational cost and modest amount of storage space. For the 3500 models of partially overlapped CHS K-joint studied, the PIM and the LIM only require 30kb and 30Mb of storage space, respectively. Furthermore, each SCF or HSS prediction could be completed within 0.02s on a low end notebook computer.

Reference

[1] Zhao, X.L., Herion, S., Packer, J.A., Puthli, R., Sedlacek, G., Wardenier, J., Weynand, K.,van Wingerde, A. and Yeomans, N., 2000. Design Guide for Circular and Rectangular hollow Section Joints under Fatigue Loading. CIDECT, TUV Germany.

[2] EN 1993, 2004a. Eurocode 3: Design of steel structures, Parts 1.9 and 1.10, CEN Central Secretariat, Rue de Stassart 36, B-1050 Brussels, BELGIUM.

[3] Chiew, S. P., Lie, S. T., Lee, C. K. and Huang Z. W., 2004. Fatigue Performance of Cracked Tubular T Joints under Combined Loads. I: Experimental, ASCE Journal of Structural Engineering, 130(4), pp. 562 - 571.

[4] Chiew, S. P., Lee, C. K., Lie, S. T. and Ji H. L., 2007. Fatigue behaviors of Square-to-Square Hollow Section T-joint with corner crack. I: Experimental studies, Engineering Fracture Mechanics, 74(5), pp. 703 – 720.

[5] Lie, S. T., Chiew, S. P., Lee, C. K. and Huang, Z. W., 2004. Fatigue Performance of Cracked Tubular T Joints under Combined Loads. II: Numerical, ASCE Journal of Structural Engineering, 130(4), pp. 572 - 581.

[6] Lee, C. K., Chiew, S. P., Lie, S. T. and Ji, H. L., 2007. Fatigue behaviors of Square-to-Square Hollow Section T-joint with corner crack. II: Numerical Modelling, Engineering Fracture Mechanics, 74(5), pp. 721 – 738.

[7] Chiew, S. P., Lie, S. T., Lee, C. K. and Huang, Z. W., 2003. Parametric Equations for Stress Intensity Factors of Cracked Tubular T&Y-Joints, Proceedings of The Thirteenth International Offshore and Polar Engineering Conference Honolulu, Hawaii, USA, May 25–30, pp. 255- 262.

[8] Shao, Y. B. Fatigue behaviour of uniplanar CHS gap K-joints under axial and in-plane bending loads. Ph.D. Thesis, Nanyang Technological University, 2004.

[9] Zienkiewicz, O. C., Taylor, R. L. and Zhu, J. Z, 2005. The Finite Element Method: Its Basis and Fundamentals. Sixth Edition, Elsevier Butterworth-Heinemann, UK.

[10] Chiew, S. P., Lee, C. K. and Lie, S. T., 2009. Research on tubular joints at Nanyang Technological University. IES Jounral Part A: Civil & Structural Engineering, 2(1), pp. 68-84.

[11] Shao, Y, B., 2006 Analysis of stress intensity factor (SIF) for cracked tubular K-joints subjected to balanced axial load, Engineering Failure Analysis, 13(1), pp 44-64

[12] Lee, C. K., Chiew, S. P., Lie, S. T., and Nguyen, T. B. N., 2010, Adaptive mesh generation procedures for thin-walled tubular structures, Finite Elements in Analysis and Design, 46, pp. 114-131.

[13] Sabih A. L, 1993, The Fatigue, Fracture and Ultimate Behaviour of Fillet Welded RHS K-Joints with gap, Ph.D. Thesis, Manchester, UK.

[14] Sopha Thong, Stress Concentration Factor and Hot Spot Stress Studies of partially overlapped Circular Hollow Section K-joints, PhD Thesis, Nanyang Technological University, 2010

[15] Fatigue Guidance Review Panel, MATSU, 1996, Fatigue Background Guidance Document, An Offshore Technology Report. By HSE Books as an Offshore Technology Report.

[16] American Petroleum Institute, API RP2A-LRFD (1993), Recommended Practice for Planning, Designing and Constructing Fixed Offshore Structures, 1st edition, Washington D.C., USA.

[17] Gulati, K. C., Wang, W. J. and Kan, D. K. Y. (1982), “An Analytical Study of Stress Concentration Effects in Multibrace Joints under Combined Loading”, Proceedings of the 14th Annual Offshore Technology Conference, OTC 4407, Houston, TX, pp. 337-355.

Appendix A: Lagrangian interpolation for trapezoidal gird

In the NPS, in order to tidy with commonly used CHS sizes, different ranges of τ are used for different values of γ (Table 1). Thus, the interpolation grid becomes a trapezoidal (Fig. A1). Now consider the evaluation of Φ at the point ($\gamma_{eval}, \tau_{eval}$) which is inside the trapezoid *1-2-3-4* with corner coordinates defined in Table A1. To construct the interpolation functions, one could start with the usual interpolation function in the γ direction so that

$$N_a(\gamma) = \frac{\gamma_b - \gamma}{\gamma_b - \gamma_a}, \quad N_b(\gamma) = \frac{\gamma - \gamma_a}{\gamma_b - \gamma_a}, \quad N_a(\gamma) + N_b(\gamma) \equiv 1 \tag{A1}$$

After Eqn. A1 is evaluated, τ_l and τ_u, the values of τ at where the line $\gamma=\gamma_{eval}$ intersects with the edges *1-2* and *4-3*, respectively, could be computed as

$$\tau_l = N_a(\gamma)\tau_{al} + N_b(\gamma)\tau_{bl} \quad and \quad \tau_u = N_a(\gamma)\tau_{au} + N_b(\gamma)\tau_{bu} \tag{A2}$$

Now the interpolation functions in the τ direction are defined as

$$N_l(\tau) = \frac{\tau_u - \tau}{\tau_u - \tau_l}, \quad N_u(\tau) = \frac{\tau - \tau_l}{\tau_u - \tau_l}, \quad N_l(\tau) + N_u(\tau) \equiv 1 \tag{A3}$$

Finally, approximated value of Φ at ($\gamma_{eval}, \tau_{eval}$), $\tilde{\Phi}(\gamma_{eval}, \tau_{eval})$, could be computed as

$$\begin{aligned} \tilde{\Phi}(\gamma_{eval}, \tau_{eval}) &= N_a(\gamma_{eval})N_l(\tau_{eval})\Phi_1 + N_b(\gamma_{eval})N_l(\tau_{eval})\Phi_2 + \\ &\quad N_b(\gamma_{eval})N_u(\tau_{eval})\Phi_3 + N_a(\gamma_{eval})N_u(\tau_{eval})\Phi_4 \\ &= N_1(\gamma_{eval}, \tau_{eval})\Phi_1 + N_2(\gamma_{eval}, \tau_{eval})\Phi_2 + N_3(\gamma_{eval}, \tau_{eval})\Phi_3 + N_4(\gamma_{eval}, \tau_{eval})\Phi_4 \end{aligned} \tag{A4}$$

Hence, the interpolation functions for the trapezoid element, which satisfy the interpolatant condition, are defined as

$$\begin{aligned} N_1(\gamma,\tau) &= N_a(\gamma)N_l(\tau), \; N_2(\gamma,\tau) = N_b(\gamma)N_l(\tau) \\ N_3(\gamma,\tau) &= N_b(\gamma)N_u(\tau), \; N_4(\gamma,\tau) = N_a(\gamma)N_u(\tau) \end{aligned} \tag{A5}$$

Nomenclature

CHS =*Circular hollow section*

HSS =*hot spot stress*

SCF =*Stress concentration factor*

FE =*Finite element*

NPS =*Numerical parametric study*

AX =*Axial loading*

IPB =*In-plane bending*

PRM =*Parametric regression method*

MLI =*Multi-dimensional Lagrangian interpolation*

PIM =*Point interpolation method*

LIM =*Line interpolation method*

NSP =*Numbers of interpolation points for LIM*

Φ_i =*Response at node i*

ξ_{eval}^{j} =*The jth parametric coordinates of evaluation point*

M =*Numbers of parameter in NPS*

$\boldsymbol{\xi_{eval}}$ =($\xi_{eval}^{1},\xi_{eval}^{2},....,\xi_{eval}^{M}$), coordinates of evaluation point

L_j^k =*1D first order Lagrangian interpolation functions of the kth parametric coordinate*

$\tilde{\Phi}\left(\boldsymbol{\xi_{eval}}\right)$ =*Approximated response at* $\boldsymbol{\xi_{eval}}$

δ_{ij} =*The Kronecker* delta *function*

h_k =*The kth edge lengths of the hyper-rectangle*

R_0 =*Radius of Chord*

L =*Length of chord*

g =*Overlap length between two braces*

t_0 =*Thickness of chord*

t_1 =*Thickness of brace*

α =*Chord length to radius ratio*

θ =*Intersection angle of the joint*

O_v =*Overlapping ratio*

β =*Brace-to-chord diameter ratio*

γ =*Chord radius to chord thickness ratio*

τ =*Brace thickness to chord thickness ratio*

SCF_{PRM} =*SCF predicted by the PRM*

SCF_{FEM} =*SCF computed by the FE method*

$E_{PRM\text{-}FEM}(SCF)$ =Relative error between SCF_{PRM} and SCF_{FEM}

SCF_{PIM} =SCF predicted by the PIM

$E_{PIM\text{-}FEM}(SCF)$ =Relative error between SCF_{PIM} and SCF_{FEM}

SCF_{AX} =SCF for the AX loading case

SCF_{IPB} =SCF for the IPB loading case

f_{AX} =Nominal stress for the AX loading case

f_{IPB} =Nominal stress for the IPB loading case

HSS_{PIM} =HSS predicted by the PIM

HSS_{FEM} =HSS computed from the FE method

HSS_{PRM} =HSS predicted by the PRM

$E_{PIM\text{-}FEM}(HSS)$ =Relative error between HSS_{PIM} and HSS_{FEM}

$E_{PRM\text{-}FEM}(HSS)$ =Relative error between HSS_{PRM} and HSS_{FEM}

φ =Driving angle to define the intersection curve

$\hat{\sigma}_{AX}(\varphi)$ =SCF distribution along the intersection curve under AX

$\hat{\sigma}_{IPB}(\varphi)$ =SCF distribution along the intersection curve under IPB

$\hat{\sigma}_{LC}(\varphi)$ =Approximated SCF distributions along the intersection curve

$\hat{\sigma}_{LC}^{FEM}(\varphi_i)$ = The extracted SCF obtained from FE solution

HSS_{LIM} =HSS predicted by the LIM

$E_{LIM\text{-}FEM}(HSS)$ =Relative error between HSS_{LIM} and HSS_{FEM}

List of Tables

List of Figures

Figure 16. Relative errors distributions of HSS obtained from the LIM, the PIM and the PRM under AX11(100kN)+IPB12 (12kNm), Curve A
(a) Through brace
(b) Chord

Figure 17. Relative errors distributions of HSS from the LIM, the PIM and the PRM under AX21 (100kN)+IPB21(12kNm), Curve B
(a) Overlap brace
(b) Chord

Figure 18. Relative errors distributions of HSS obtained from the LIM, the PIM and the PRM under AX21 (100kN)+IPB22(12kNm), Curve A
(a) Through brace
(b) Overlap brace

Figure 19. Comparison of HSS predictions obtained from the PRM, the PIM and the LIM under AX21(100kN)+IPB21(6kNm), Curve B
(Geometrical properties of joint: $\theta = 35°$, $O_v = 0.35$, $\beta = 0.65$, $\gamma = 10.92$ and $\tau = 0.504$.)
(a) HSS distribution from the FE analyses for AX21(100kN), Chord side of Curve B
(b) HSS distribution from the FE analyses for IPB21(6kN), Chord side of Curve B
(c) HSS prediction from different methods, Chord side of Curve B

Figure 20. Extraction of SCF by extrapolation from the FE mesh

Figure 21. Organization of multilayered database for SCF in the LIM

Figure A1. Interpolation over a trapezoidal grid

Parameter	Numbers of values used	Values of parameters used in the NPS
θ	5	30°, 40°, 45°, 50°,60°
O_v	5	0.25, 0.4, 0.5, 0.6, 0.75
β	7	0.4, 0.5, 0.6, 0.7, 0.8, 0.9, 1.0
γ	5	17.06, 11.38, 8.53, 6.83, 5.46
τ	4	For γ=17.06, τ= 0.65, 0.75, 0.85, 1.0
		For γ=11.38, τ= 0.5, 0.6, 0.8, 1.0
		For γ=8.53, τ= 0.38, 0.5, 0.75, 1.0
		For γ=6.83, τ= 0.3, 0.6, 0.8, 1.0
		For γ=5.46, τ= 0.32, 0.64, 0.8, 1.0

Table 1. Geometrical parameters used in the NPS

Load Cases	Members and curves	Frequency of occurrence of SCF P/R ratio (%)		
		P/R<0.8	0.8≤P/R≤1.5	P/R>1.5
AX11	Though brace: AX11tC	4.17	85.82	10.00
	Chord: AX11cC	4.97	73.22	21.80
AX21	Overlap brace: AX21oB	3.29	78.23	18.48
	Chord: AX21cB	3.40	76.66	19.94
IPB11	Though brace: IPB11tC	2.57	88.75	8.68
	Chord: IPB11cC	4.20	70.45	25.35
IPB12	Though brace: IPB12tA	3.48	84.8	11.71
	Overlap brace: IPB12oA	1.29	89.65	9.06
IPB21	Overlap brace: IPB21oB	1.20	86.92	11.88
	Chord: IPB21cB	3.23	72.45	24.32
IPB22	Overlap brace: IPB22oA	3.97	85.54	10.48
	Though brace: IPB22tA	1.09	90.54	8.37

Table 2. Assessment of the empirical SCF equations by the P/R ratios

Parameters	Numbers of values used	Values of parameters used
θ	2	35°, 55°
O_v	4	0.35, 0.45, 0.55, 0.65
β	6	0.45, 0.55, 0.66, 0.75, 0.85, 0.95
γ	2	9.75, 13.65
τ	2	For γ=9.75, τ=0.71, 0.86
	Total=2×4×6×2×2=192	For γ=1.65, τ=0.6, 0.63

Table 3. Geometrical parameters of the 192 mid-point models

Load Cases	Members and curves	Frequency of occurrence of $E_{PRM\text{-}FEM}$ (%)		
		$E_{PRM\text{-}FEM}$ <-20%	-20%≤$E_{PRM\text{-}FEM}$ ≤20%	$E_{PRM\text{-}FEM}$ >20%
AX11	Though brace: AX11tC	1.97	92.11	5.92
	Chord: AX11cC	0.66	44.74	54.61
AX21	Overlap brace: AX21oB	5.26	68.42	26.32
	Chord: AX21cB	9.21	85.53	5.26
IPB11	Though brace: IPB11tC	7.89	87.50	4.61
	Chord: IPB11cC	23.68	69.08	10.53
IPB12	Though brace: IPB12tA	5.92	88.16	5.92
	Overlap brace: IPB12oA	6.58	88.16	5.26
IPB21	Overlap brace: IPB21oB	8.55	85.53	5.92
	Chord: IPB21cB	13.03	69.21	17.76
IPB22	Overlap brace: IPB22oA	3.95	80.92	15.13
	Though brace: IPB22tA	4.61	94.08	1.32

Table 4. Distributions of $E_{PRM\text{-}FEM}$ for the PRM

Load Cases	Members and curves	Frequency of occurrence of $E_{PIM\text{-}FEM}$ (%)		
		$E_{PIM\text{-}FEM}$ <-20%	-20%≤$E_{PIM\text{-}FEM}$ ≤20%	$E_{PIM\text{-}FEM}$ >20%
AX11	Though brace: AX11tC	0	99.35	0.65
	Chord: AX11cC	0	99.35	0.65
AX21	Overlap brace: AX21oB	1.96	96.08	1.96
	Chord: AX21cB	0.27	99.08	0.65
IPB11	Though brace: IPB11tC	0	99.35	0.65
	Chord: IPB11cC	0.65	98.70	0.65
IPB12	Though brace: IPB12tA	0	99.35	0.65
	Overlap brace: IPB12oA	0	99.35	0.65
IPB21	Overlap brace: IPB21oB	0	99.35	0.65
	Chord: IPB21cB	0	99.35	0.65
IPB22	Overlap brace: IPB22oA	0	99.35	0.65
	Though brace: IPB22tA	0	99.35	0.65

Table 5. Distributions of $E_{PIM\text{-}FEM}$ for the PIM

Methods	Load Cases	Curves	Members	Frequency of occurrence of reltive errors $E_{PRM-FEM}$, $E_{PIM-FEM}$, $E_{LIM-FEM}$ (%)		
				< -20.00	**-20.0 ↔ 20.0**	**> 20.00**
PRM (Eqn. 12b)	AX11(100kN) +IPB11(12kNm)	C	Through brace	3.27	95.42	1.31
			Chord	10.46	79.74	9.80
	AX11(100kN) +IPB12(12kNm)	A	Through brace	3.27	89.54	7.19
			Overlap brace	7.19	87.58	5.23
	AX21(100kN) +IPB21(12kNm)	B	Overlap brace	3.27	95.42	1.31
			Chord	10.46	71.24	18.30
	AX21(100kN) +IPB22(12kNm)	A	Through brace	0.61	96.73	2.61
			Overlap brace	3.92	95.42	0.65
PIM (Eqn. 12a)	AX11(100kN) +IPB11(12kNm)	C	Through brace	0.66	92.76	6.58
			Chord	1.32	96.71	1.97
	AX11(100kN) +IPB12(12kNm)	A	Through brace	0.66	96.05	3.29
			Overlap brace	-	96.71	3.29
	AX21(100kN) +IPB21(12kNm)	B	Overlap brace	0.65	96.73	2.61
			Chord	0.65	88.24	11.11
	AX21(100kN) +IPB22(12kNm)	A	Through brace	0.65	95.42	3.92
			Overlap brace	0.65	97.39	1.96
LIM (Eqn. 15)	AX11(100kN) +IPB11(12kNm)	C	Through brace	-	96.05	3.95
			Chord	0.63	98.05	1.32
	AX11(100kN) +IPB12(12kNm)	A	Through brace	0.66	96.71	2.63
			Overlap brace	0.66	98.03	1.97
	AX21(100kN) +IPB21(12kNm)	B	Overlap brace	0.65	96.73	2.61
			Chord	0.61	97.08	2.31
	AX21(100kN) +IPB22(12kNm)	A	Through brace	0.65	95.42	3.92
			Overlap brace	0.65	97.39	1.96

Table 6. Distributions of the relative errors for HSS predictions

Node	Coordinates	Nodal Value
1	(γ_a, τ_{al})	Φ_1
2	(γ_b, τ_{bl})	Φ_2
3	(γ_b, τ_{bu})	Φ_3
4	(γ_a, τ_{au})	Φ_4

Table 1A Coordinates of trapezoid

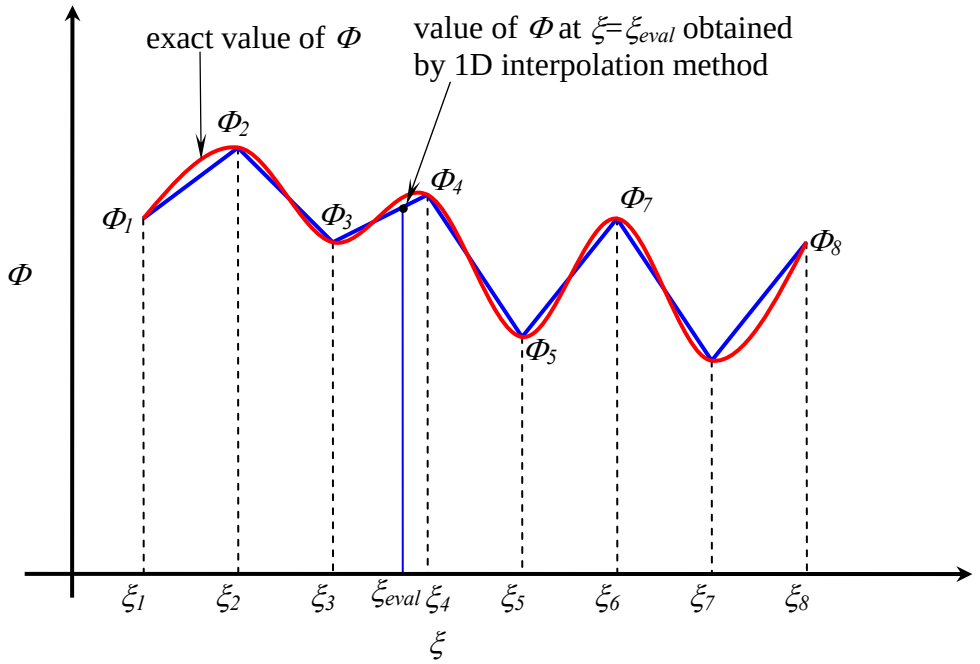

Figure 1. The interpolation method in 1D with a single parameter ξ

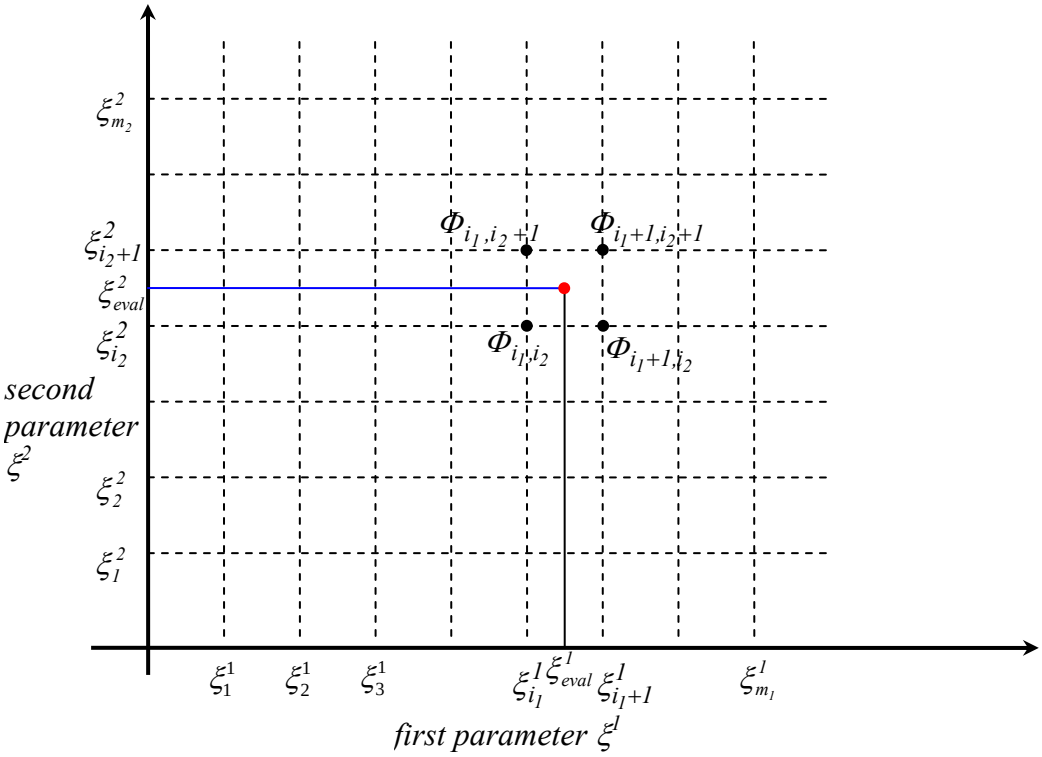

Figure 2. The interpolation method in 2D with parameters ξ^1 and ξ^2

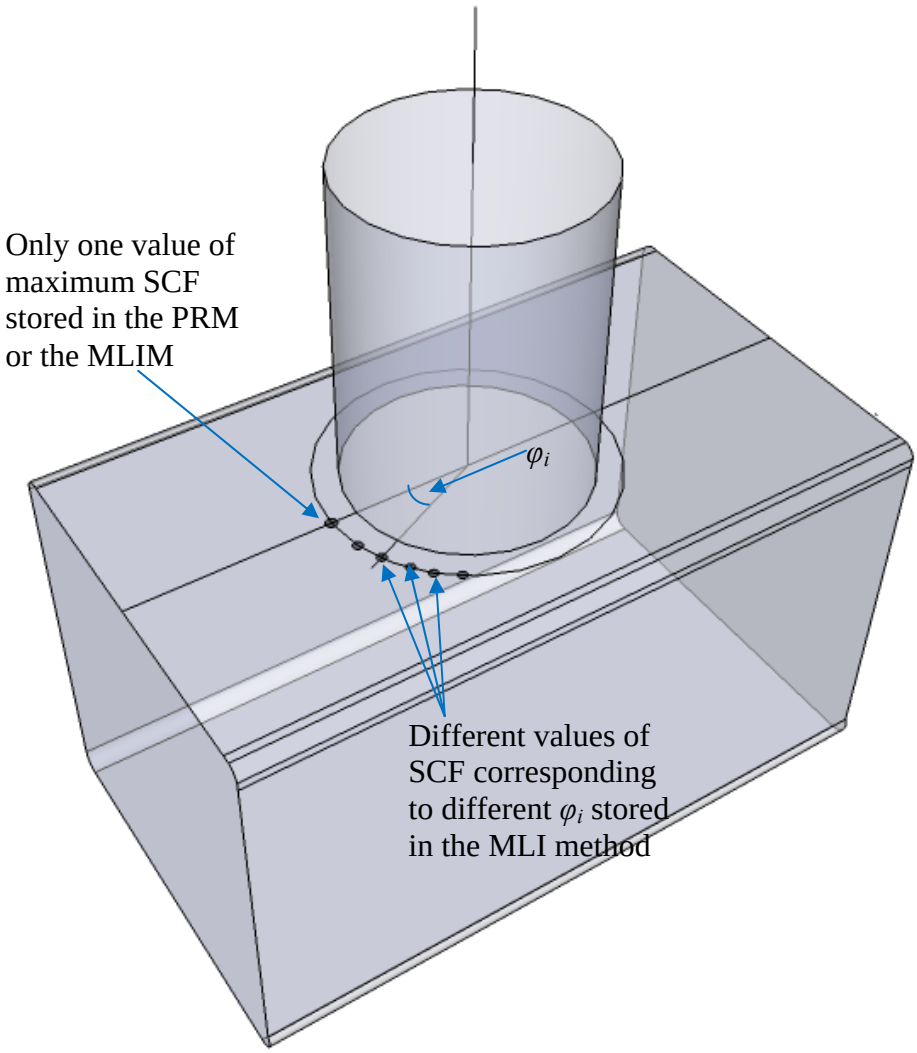

Figure 3. Single and multiple SCF values of a tubular joint stored in the MLIM

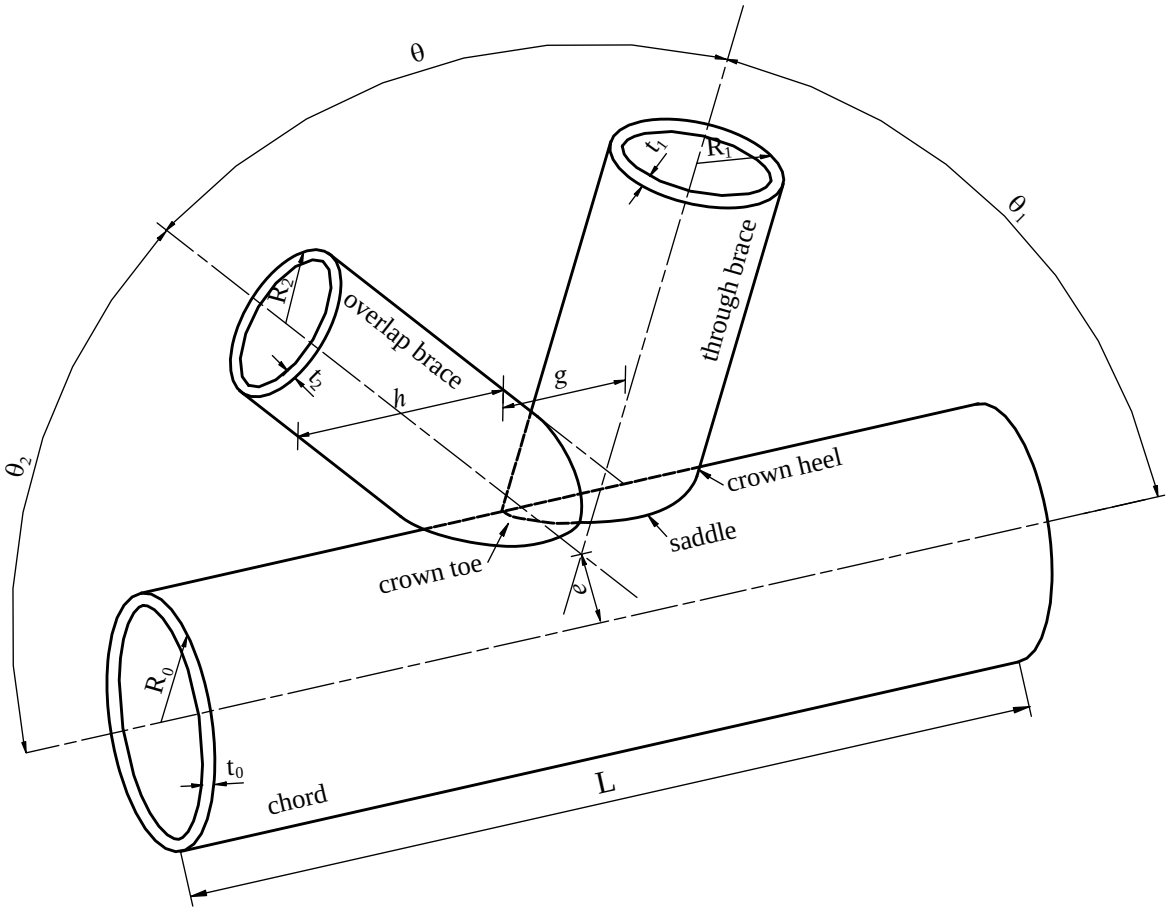

$$\alpha = \frac{L}{R_0}, \gamma = \frac{R_0}{t_0}, O_v = \frac{g}{R_0}, \beta_1 = \frac{R_1}{R_0}, \tau_1 = \frac{t_1}{t_0}, \beta_2 = \frac{R_2}{R_0}, \tau_2 = \frac{t_2}{t_0}$$

Figure 4 Geometrical parameters for a partially overlapped CHS K-joint

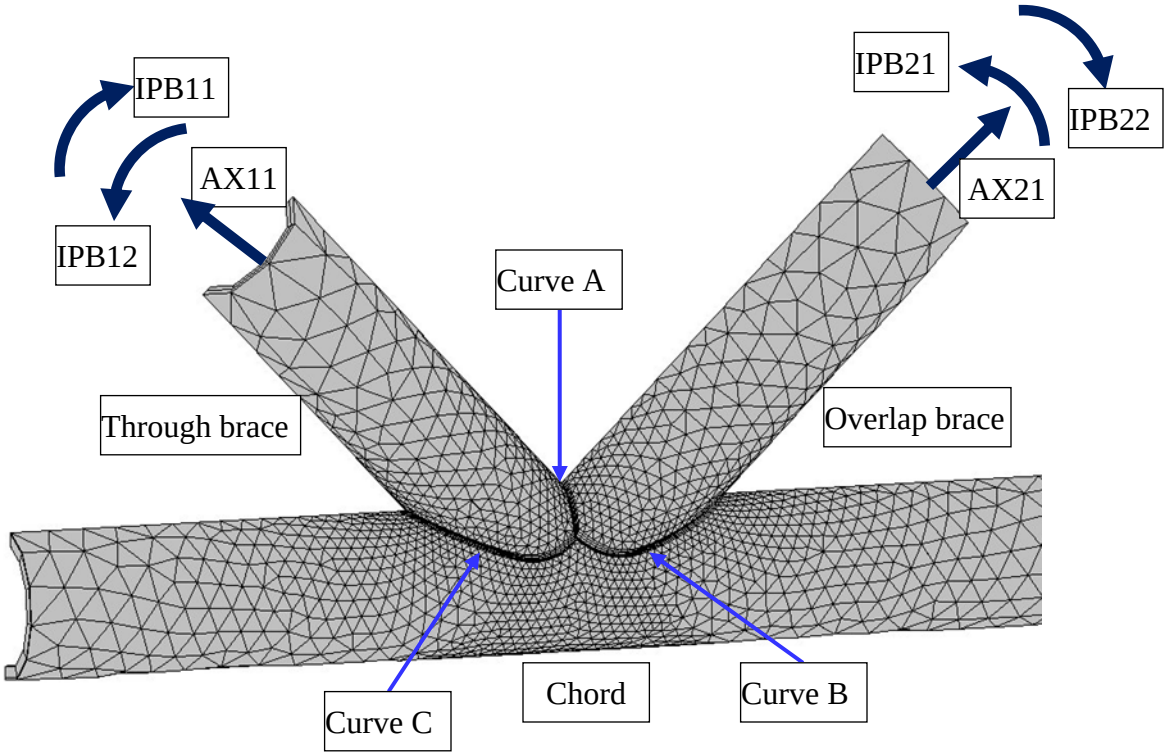

Figure 5. Basic loading cases, definitions of the intersection Curves A, B and C and typical FE mesh used in the NPS

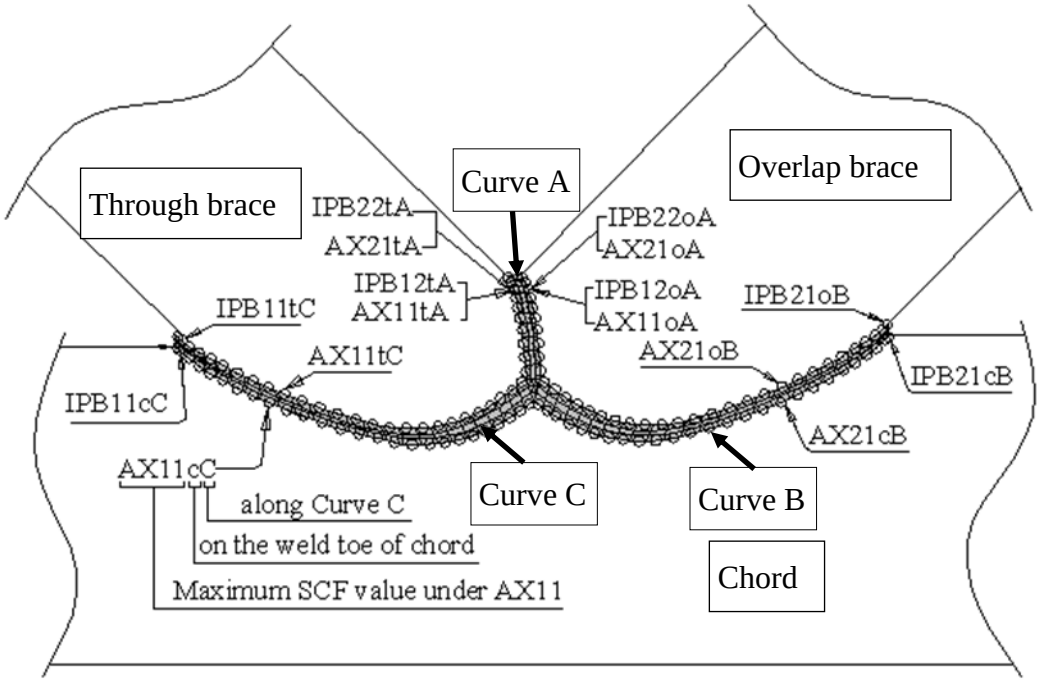

Figure 6. Definitions of the sixteen maximum SCF stored along the three intersection curves

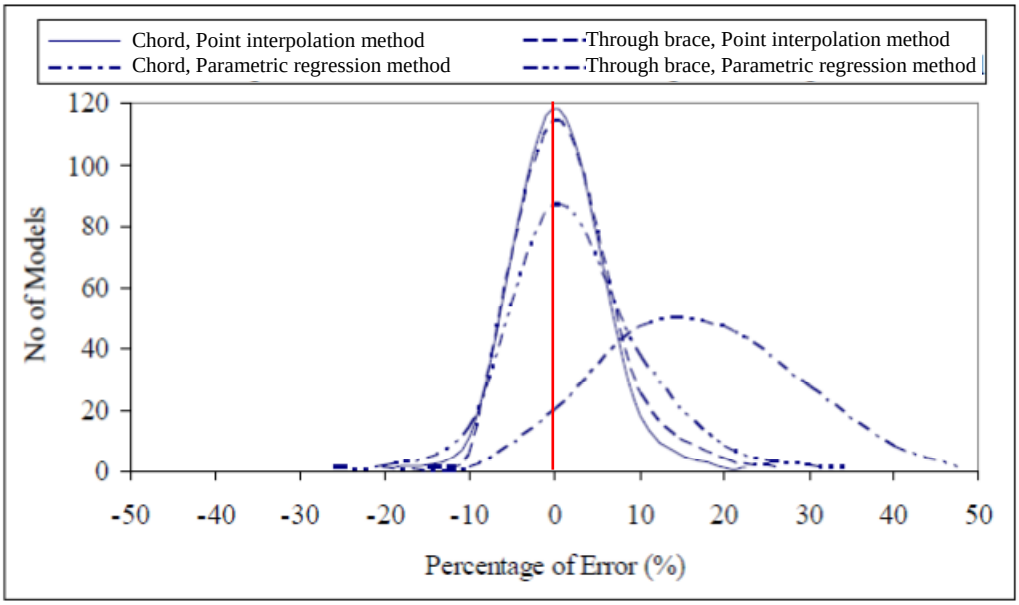

Figure 7. Relative errors distributions of SCF for the mid-point models, AX11, Curve C (AX11tC and AX11cC)

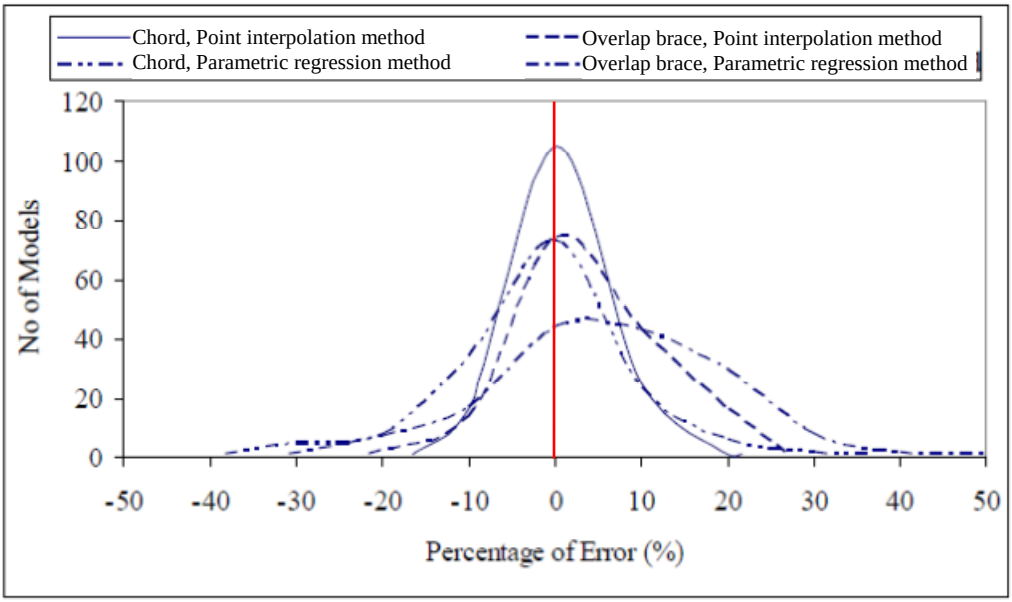

Figure 8. Relative errors distributions of SCF for the mid-point models, AX21, Curve B (AX21oB and AX21cB)

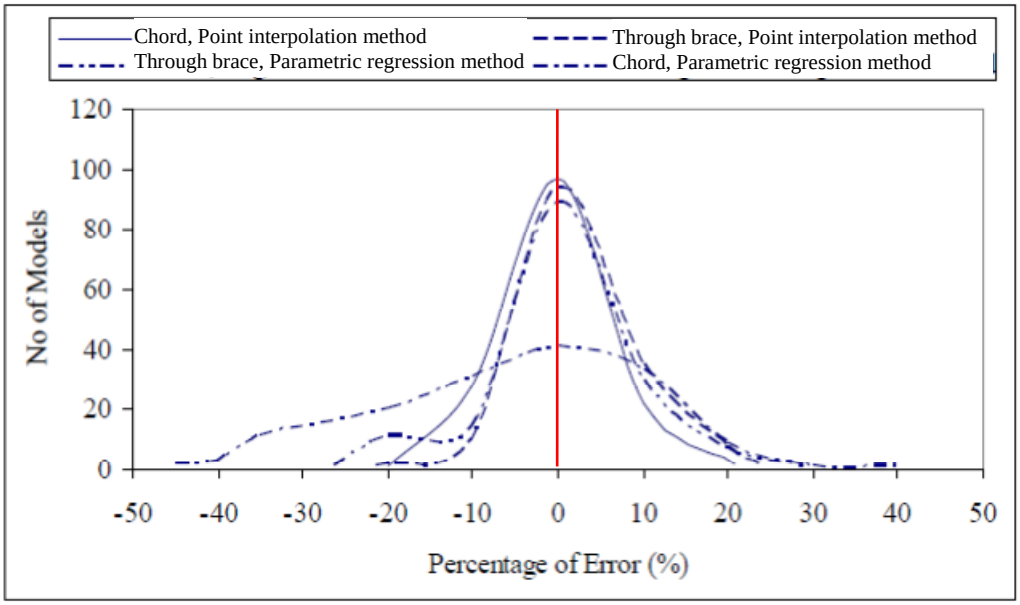

Figure 9. Relative errors distributions of SCF for the mid-point models, IPB11, Curve C (IPB11tC and IPB11cC)

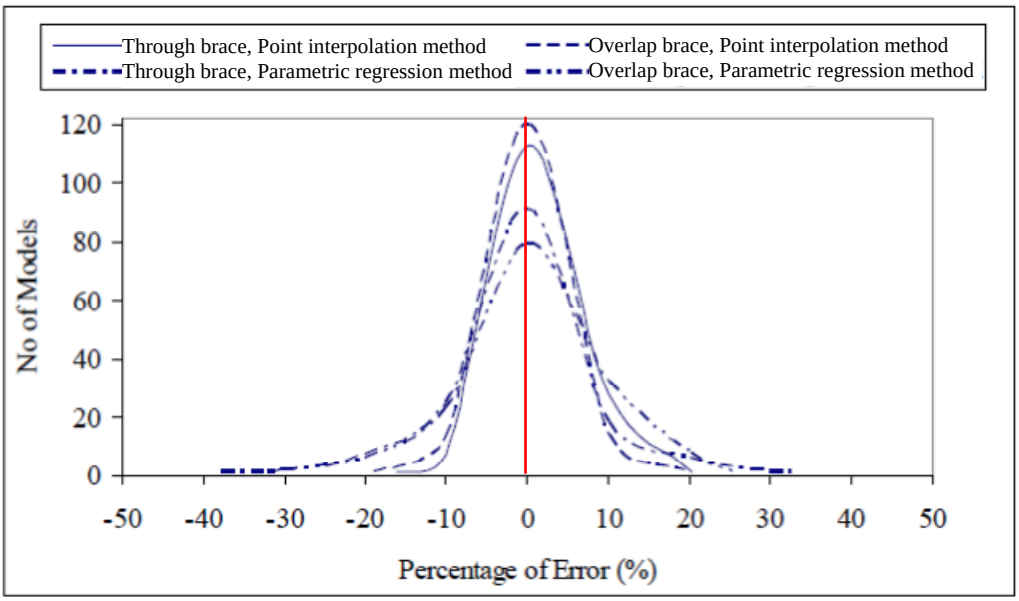

Figure 10. Relative errors distributions of SCF for the mid-point models, IPB12, Curve A (IPB12tA and IPB12oA)

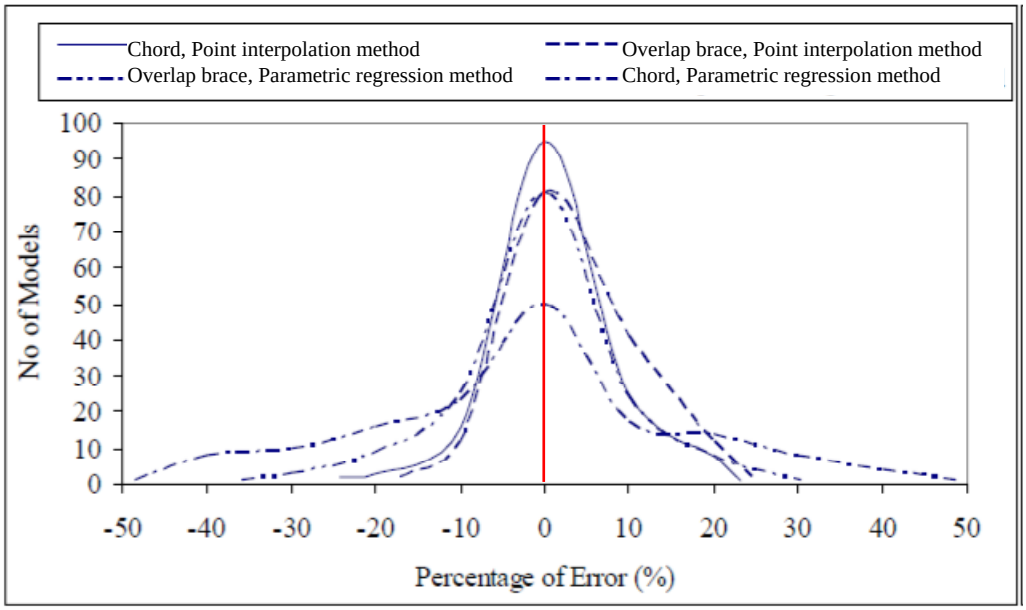

Figure 11. Relative errors distributions of SCF for the mid-point models, IPB21, Curve B (IPB21oB and IPB21cB)

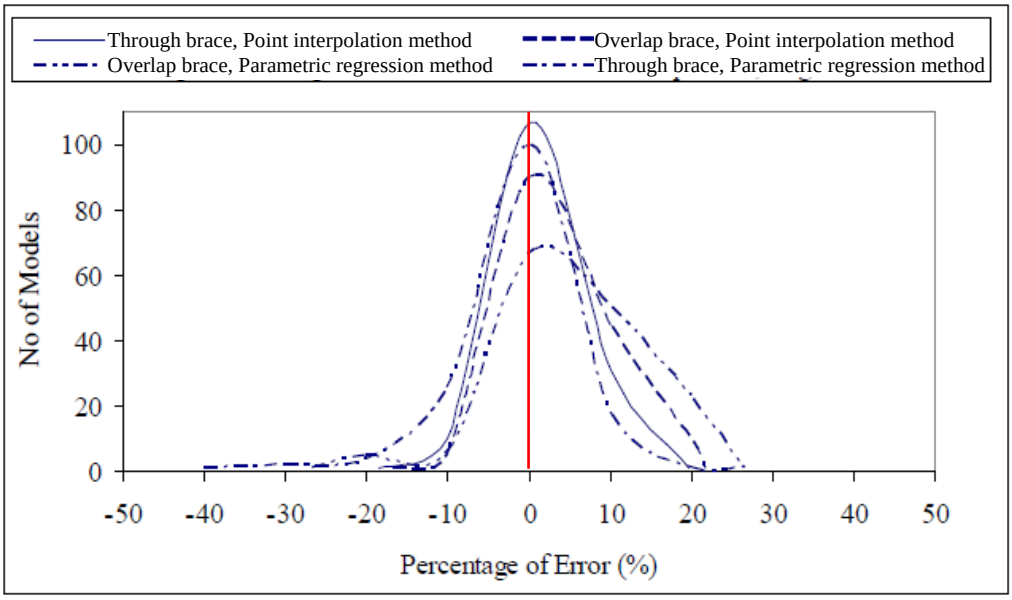

Figure 12. Relative errors distributions of SCF for the mid-point models, IPB22, Curve A (IPB22tA and IPB22oA)

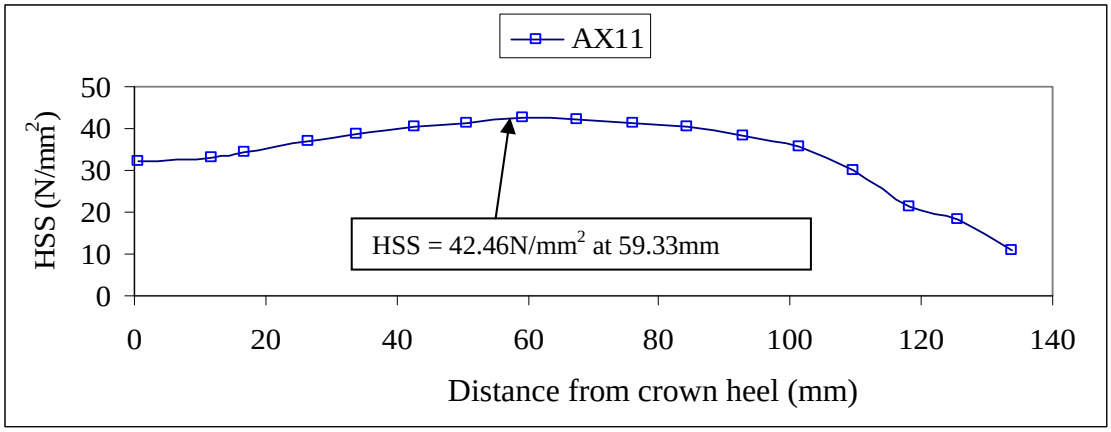

(a) HSS under AX11(100kN) along Curve C, Chord side

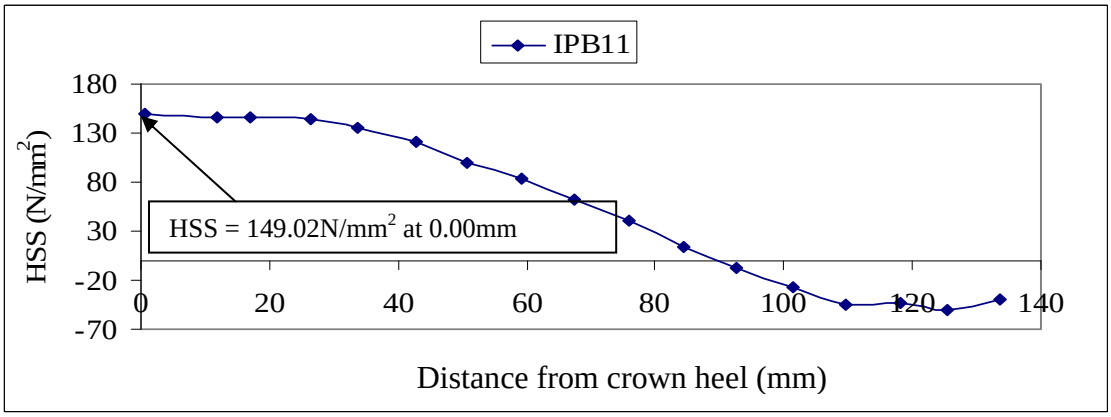

(b) HSS under IPB11(12kNm) along Curve C, Chord side

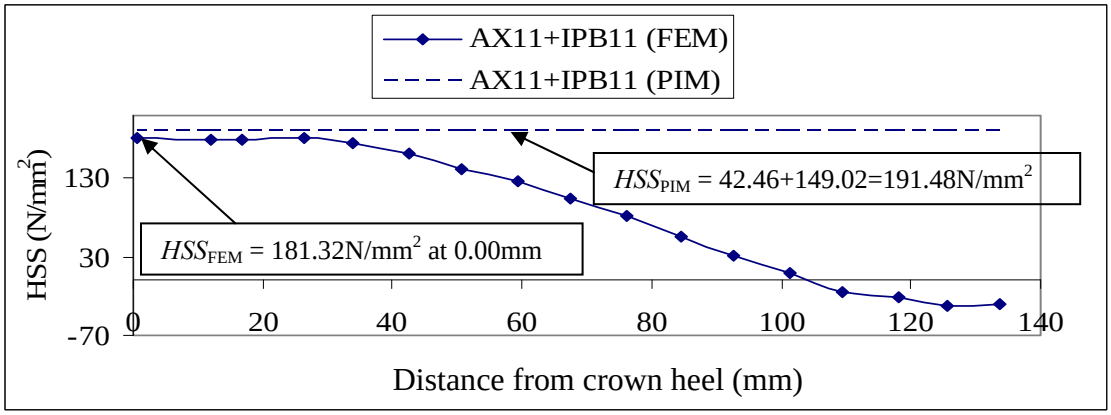

(c) HSS under AX11(100kN)+IPB11(12kNm) along Curve C, Chord side

Figure 13. HSS estimations for AX11(100kN)+IPB11(12kNm) by the FEM and the PIM (Geometrical properties of the joint: $\theta = 60°$, $O_v = 0.25$, $\beta = 0.4$, $\gamma = 11.38$ and $\tau = 0.8$.)

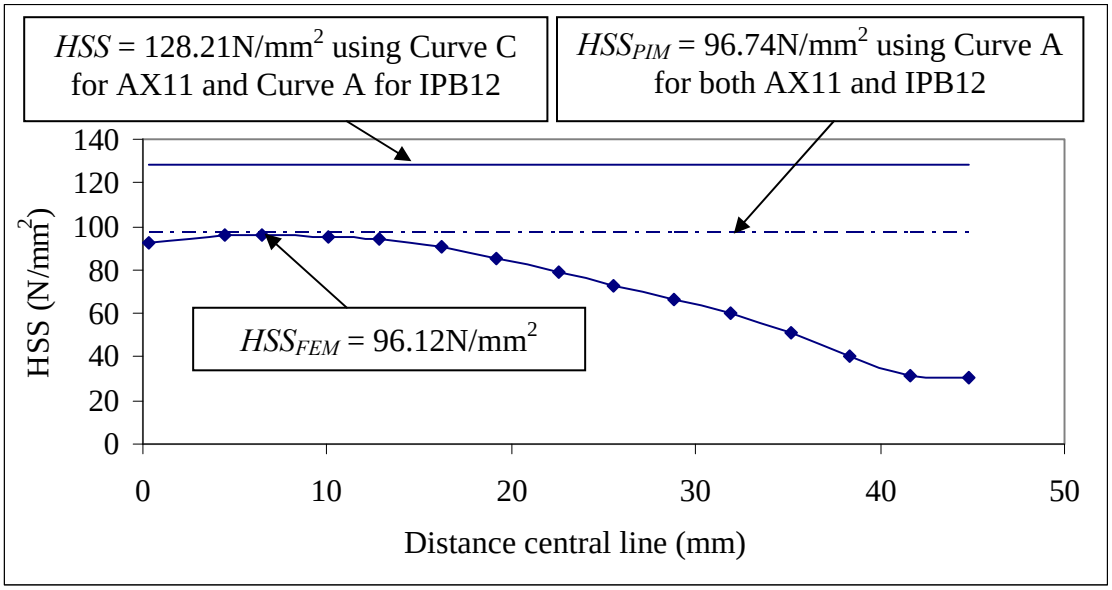

Figure 14. HSS under AX11 (100kN)+IPB12(12kNm) from FE analysis and different approaches of the PIM
(Geometrical properties of the joint: $\theta = 60°$, $O_v = 0.25$, $\beta = 0.4$, $\gamma = 11.38$ and $\tau = 0.8$.)

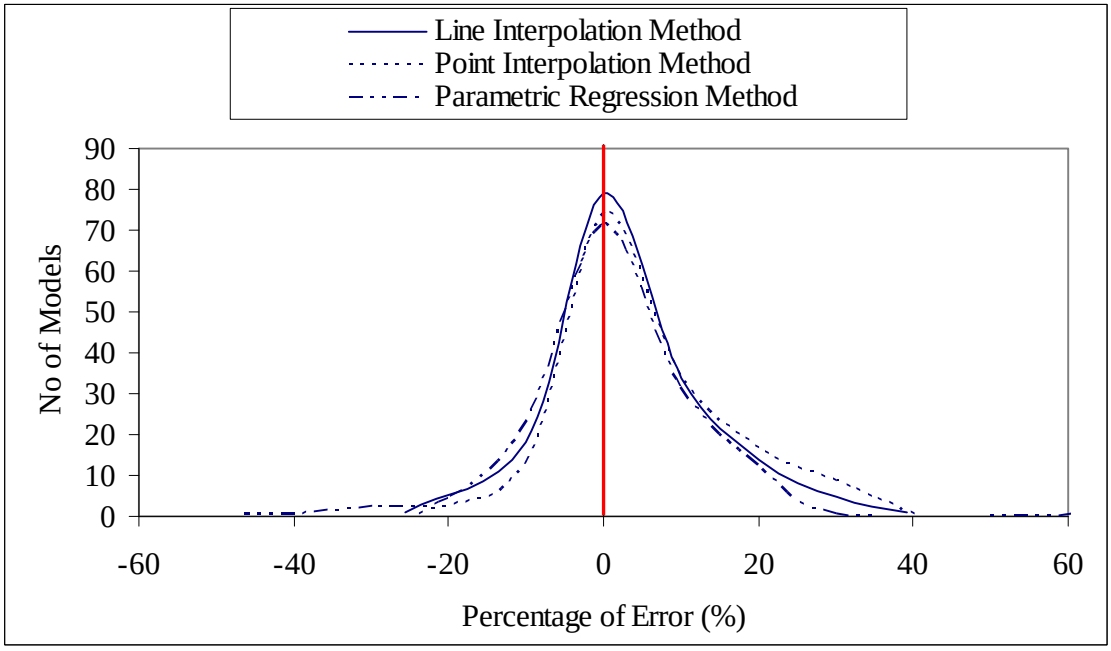

(a) Through brace

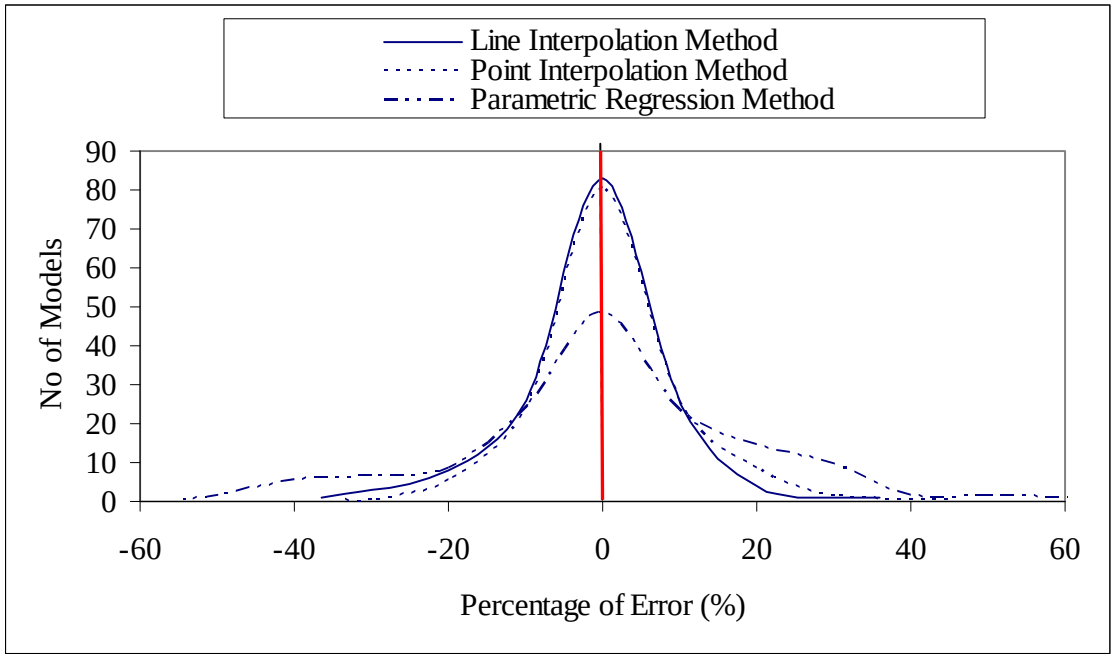

(b) Chord

Figure 15. Relative errors distributions of HSS obtained from the LIM, the PIM and the PRM under AX11 (100kN)+IPB11(12kNm), Curve C

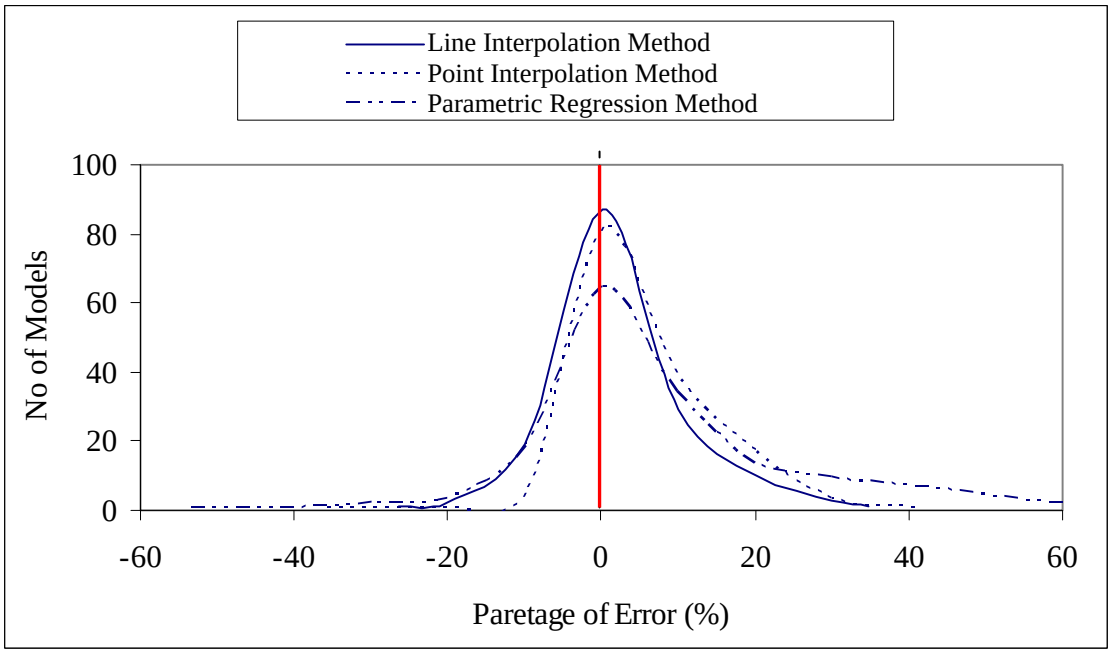

(a) Through brace

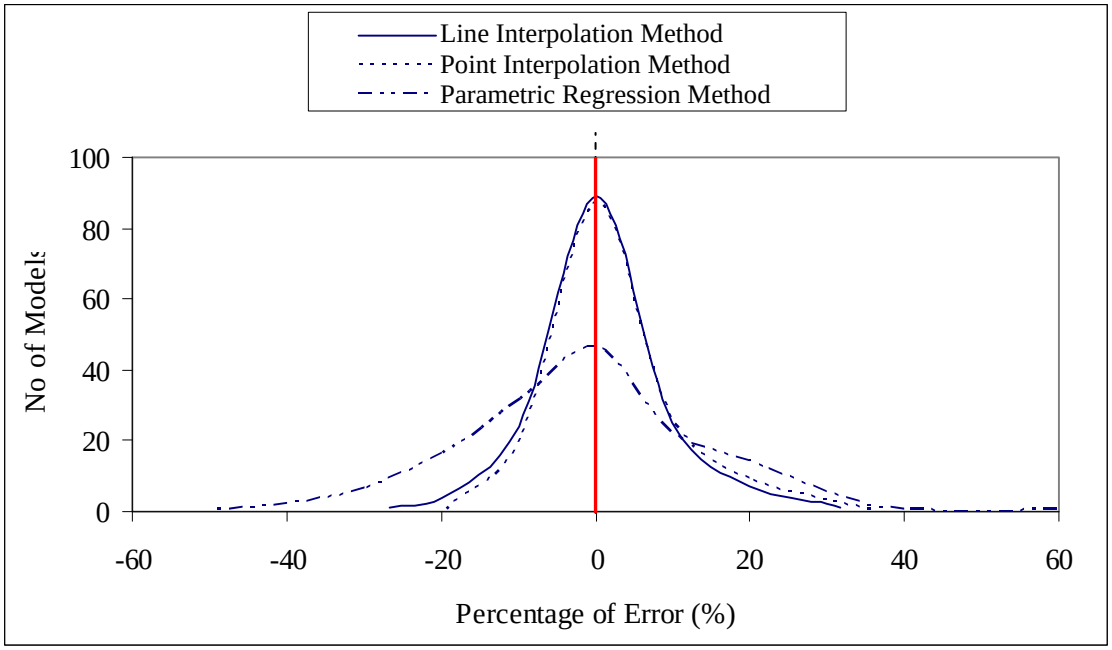

(b) Overlap brace

Figure 16. Relative errors distributions of HSS obtained from the LIM, the PIM and the PRM under AX11(100kN)+IPB12 (12kNm), Curve A

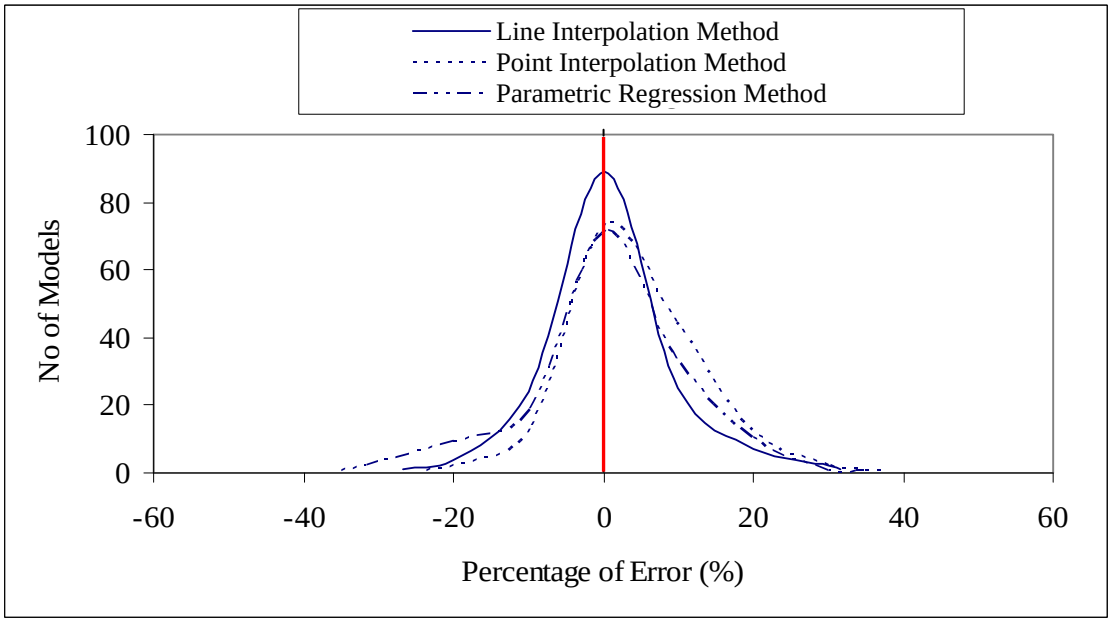

(a) Overlap brace

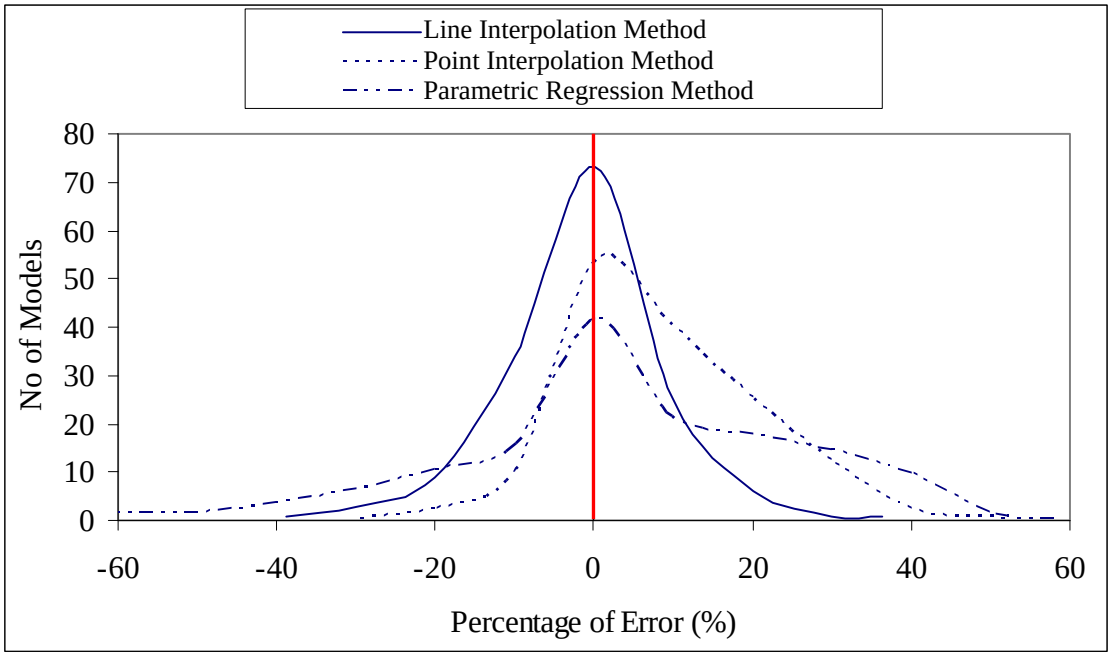

(b) Chord

Figure 17. Relative errors distributions of HSS from the LIM, the PIM and the PRM under AX21 (100kN)+IPB21(12kNm), Curve B

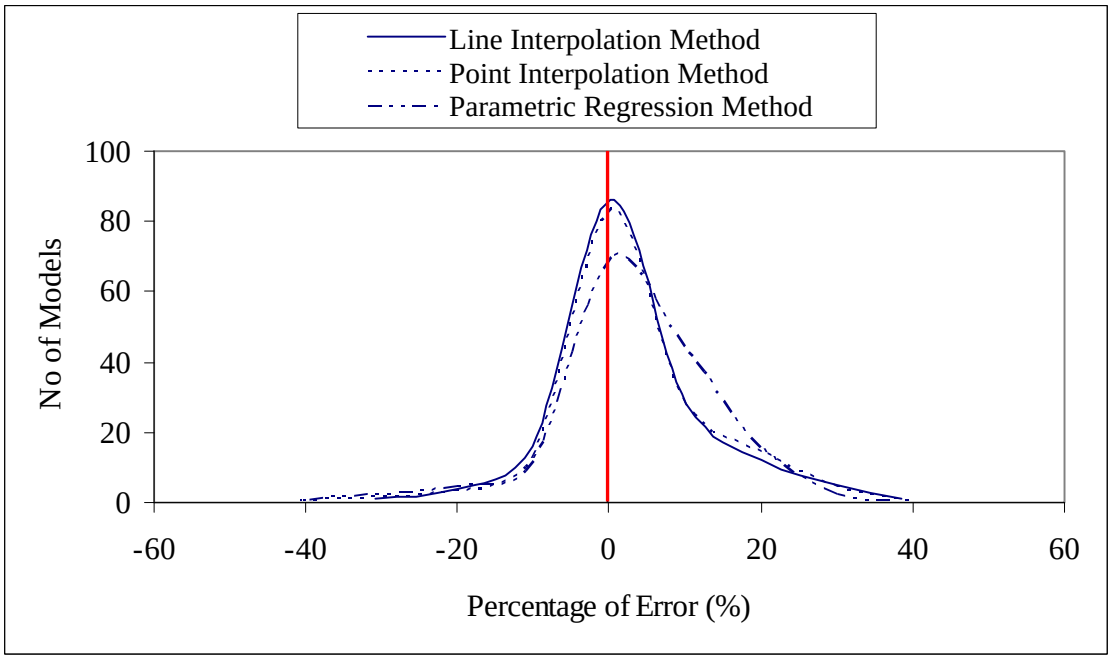

(a) Through brace

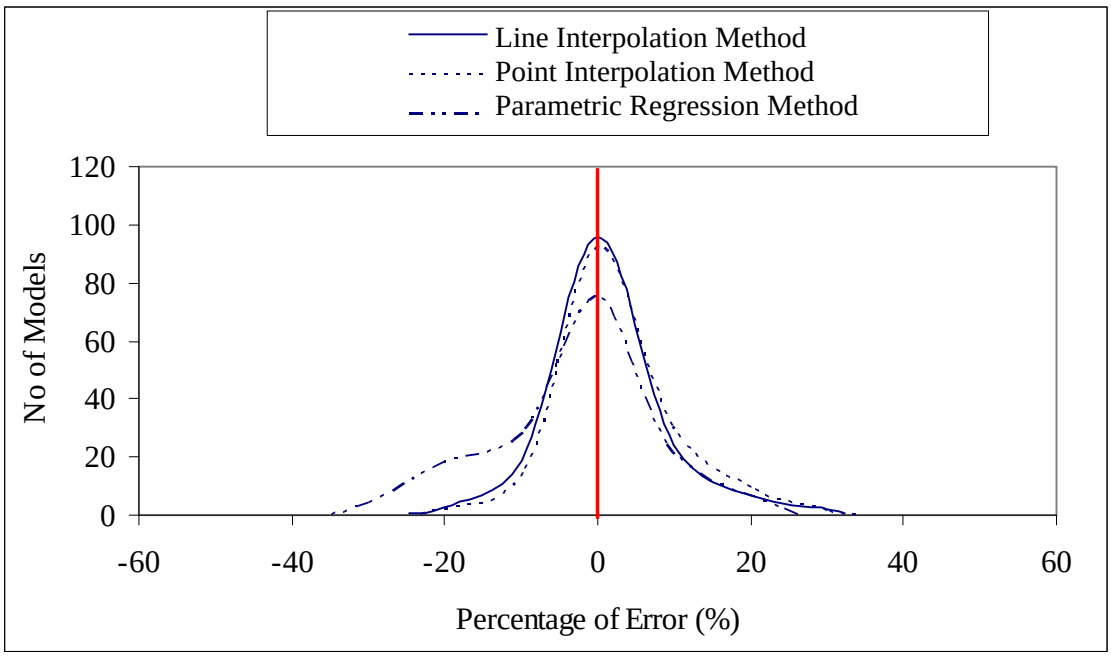

(b) Overlap brace

Figure 18. Relative errors distributions of HSS obtained from the LIM, the PIM and the PRM under AX21 (100kN)+IPB22(12kNm), Curve A

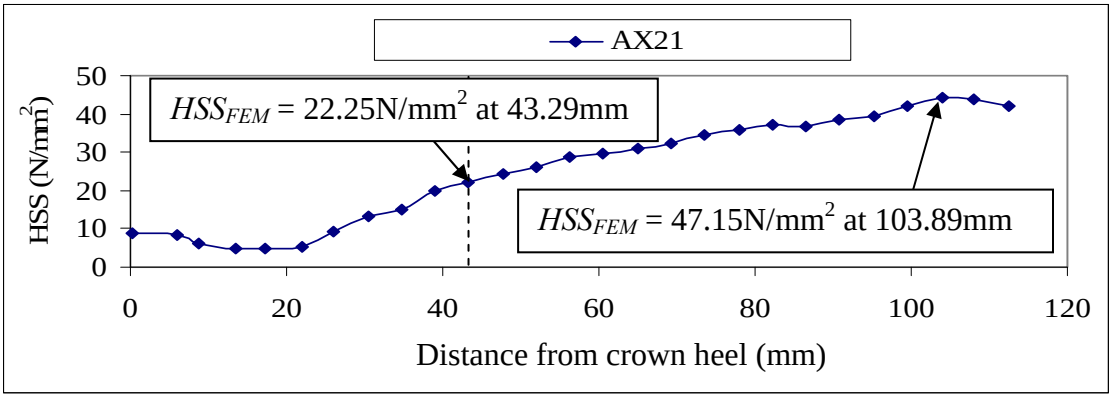

(a) HSS distribution from the FE analyses for AX21(100kN), Chord side of Curve B

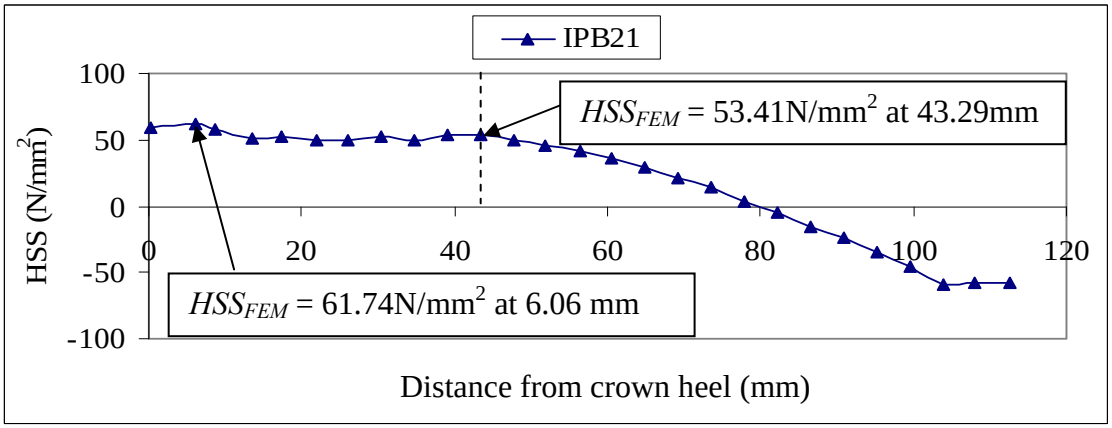

(b) HSS distribution from the FE analyses for IPB21(6kN), Chord side of Curve B

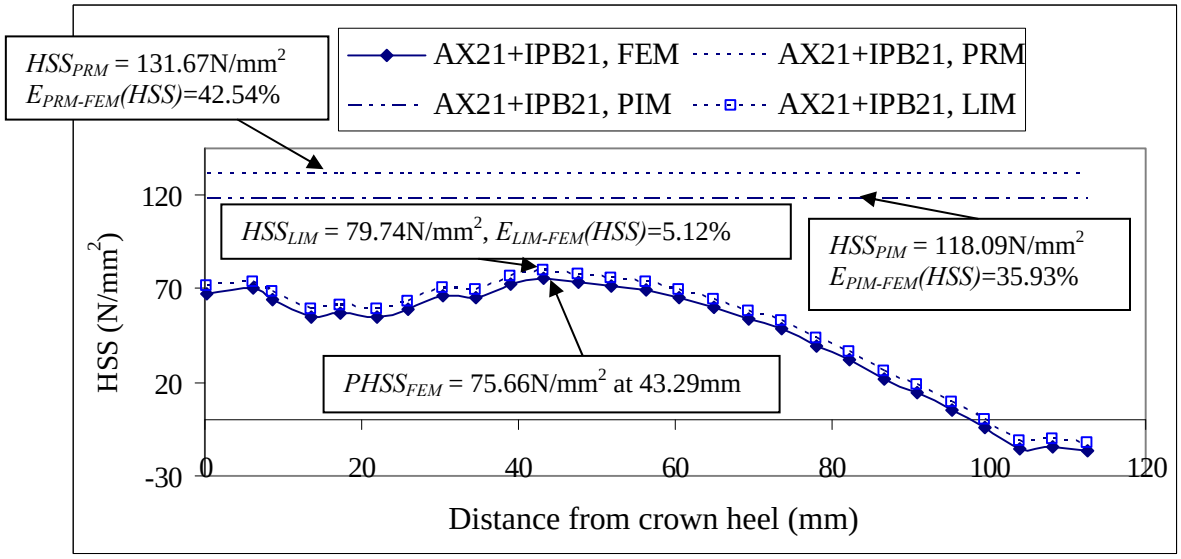

(c) HSS prediction from different methods, Chord side of Curve B

Figure 19. Comparison of HSS predictions obtained from the PRM, the PIM and the LIM under AX21(100kN)+IPB21(6kNm), Curve B

(Geometrical properties of joint: $\theta = 35°$, $O_v = 0.35$, $\beta = 0.65$, $\gamma = 10.92$ and $\tau = 0.504$.)

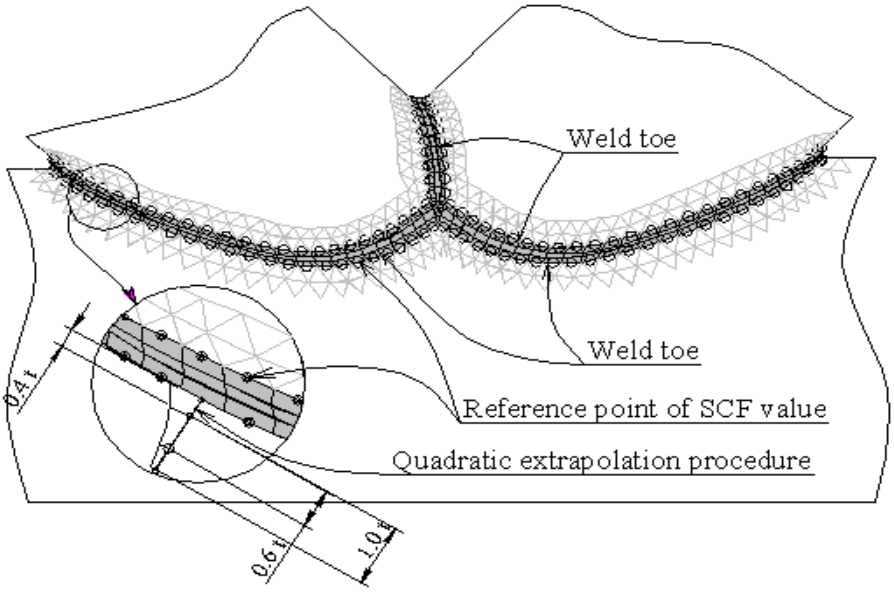

Figure 20. Extraction of SCF by extrapolation from the FE mesh

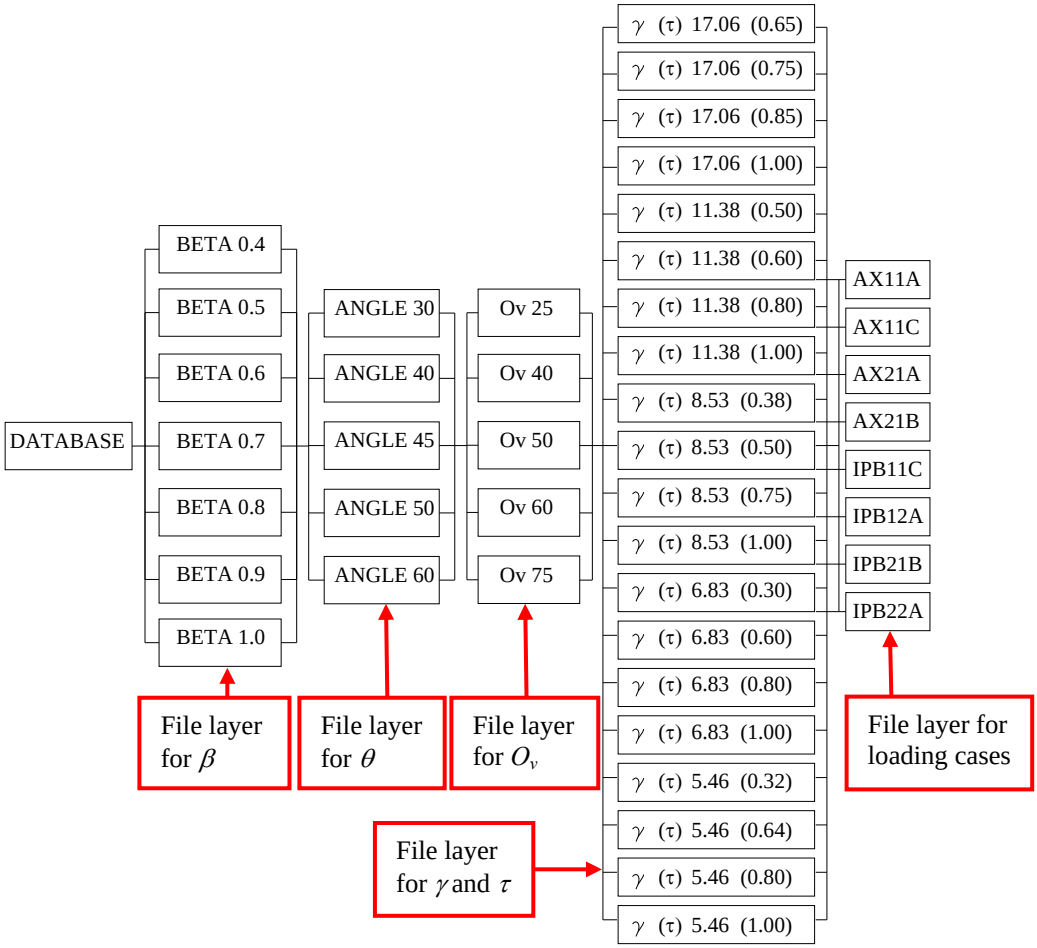

Figure 21. Organization of multilayered database for SCF in the LIM

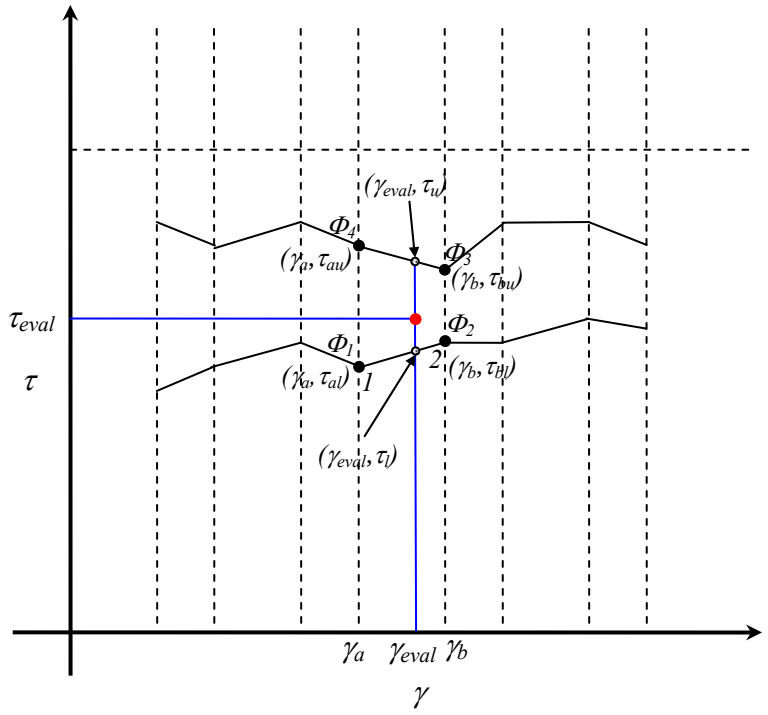

Figure A1. Interpolation over a trapezoidal grid